Title

Seasonal Transitions and the Westerly Jet in the Holocene East Asian Summer Monsoon

Journal

Journal of Climate, 30(9)

ISSN

0894-8755

Authors

Kong, Wenwen
Swenson, Leif M
Chiang, John CH

Publication Date

2017-05-01

DOI

10.1175/jcli-d-16-0087.1

Peer reviewed

Seasonal Transitions and the Westerly Jet in the Holocene East Asian Summer Monsoon

WENWEN KONG, LEIF M. SWENSON,[a] AND JOHN C. H. CHIANG

Department of Geography and Berkeley Atmospheric Sciences Center, University of California, Berkeley, Berkeley, California

a. Current affiliation: Department of Land, Air, and Water Resources, University of California, Davis, Davis, California.

Corresponding author e-mail: Wenwen Kong, wenwen.kong@ berkeley.edu

Abstract

The Holocene East Asian summer monsoon (EASM) was previously characterized as a trend toward weaker monsoon intensity paced by orbital insolation. It is demonstrated here that this evolution is more accurately characterized as changes in the transition timing and duration of the EASM seasonal stages (spring, pre-mei-yu, mei-yu, midsummer), and tied to the north–south displacement of the westerlies relative to Tibet. To this end, time-slice simulations across the Holocene are employed using an atmospheric general circulation model. Self-organizing maps are used to objectively identify the transition timing and duration of the EASM seasonal stages.

Compared to the late Holocene, an earlier onset of mei-yu and an earlier transition from mei-yu to midsummer in the early to mid-Holocene are found, resulting in a shortened mei-yu and prolonged midsummer stage. These changes are accompanied by an earlier northward positioning of the westerlies relative to Tibet. Invoking changes to seasonal transitions also provides a more satisfactory explanation for two key observations of Holocene East Asian climate: the “asynchronous Holocene optimum” and changes to dust emissions.

A mechanism is proposed to explain the altered EASM seasonality in the simulated early to mid-Holocene. The insolation increase over the boreal summer reduces the pole–equator temperature gradient, leading to northward-shifted and weakened westerlies. The meridional position of the westerlies relative to the Tibetan Plateau determines the onset of mei-yu and possibly the onset of the midsummer stage. The northward shift in the westerlies triggers earlier seasonal rainfall transitions and, in particular, a shorter mei-yu and longer midsummer stage.

Keywords: Asia; Rainbands; Jets; Monsoons; Paleoclimate; Seasonal variability

1. Introduction

Unlike other major monsoon systems (such as the West African monsoon and the North American monsoon), the East Asian summer monsoon (EASM) undergoes unique meridional transitions during its seasonal evolution (Lau et

al. 1988; Tao and Chen 1987) characterized by three quasi-stationary stages and two abrupt jumps between them (Ding and Chan 2005). In their review article, Ding and Chan (2005) suggested that the onset process of the EASM can be summarized as follows: 1) Following the “spring persistent rainfall” (Wu et al. 2007), the first onset starts in early May, which we label as the “pre-mei-yu” season. 2) The rainfall band then advances northward in mid-June, forming the Chinese mei-yu, the Korean changma, and the Japanese baiu. 3) The second jump occurs around mid-July, bringing more rainfall over northern China, which we label as “midsummer rainfall,” following Xu and Zipser (2011). The conventional interpretation of the EASM seasonal evolution is that the land–sea thermal contrast caused by the differential heat capacities of the Asian continent and the Pacific Ocean induces a pressure contrast, which in turn drives a low-level monsoonal flow from the South China Sea that penetrates inland, bringing moisture and thus rainfall. This mechanism is thought to contribute to the onset and interannual variability of the EASM (e.g., Li and Yanai 1996). The thermal and mechanical effects of the Tibetan Plateau are also thought to play important roles in the EASM evolution (Molnar et al. 2010; Yanai and Wu 2006).

Previous work provided a basis to link the seasonal migration of the modern EASM and that of the midlatitude westerlies impinging on the Tibetan Plateau. The meridional migration of the westerlies relative to Tibet follows the seasonal cycle of the insolation and its effect on the meridional temperature gradient, consistent with the thermal wind relationship. The advance of the westerly jet over East Asia was first tied to the downstream northward transition of the rainfall belt over China in the English literature in the 1950s (Staff 1957, 1958a,b; Yeh et al. 1959). Subsequent studies have further supported the synchronous connection between the westerlies shift in the Tibetan region and the seasonal transitions of the EASM. For example, Schiemann et al. (2009) show that the position of the westerly jet impinging on the Tibetan Plateau is systematically correlated to the spatial distribution of precipitation over East Asia: the climatological westerly jet stays to the south of the Tibetan Plateau in April and migrates onto the Tibetan Plateau in May, corresponding to the pre-mei-yu season; the jet reaches the northern edge of the Tibetan Plateau in June timed to the start of the mei-yu season; the northernmost jet position is achieved in July to August, timed with the midsummer rainfall season; and finally, the jet retreats southward and the East Asian monsoonal rainfall declines in September.

This synchronous relationship points to a strong dynamical control of the westerlies on EASM seasonality (e.g., Liang and Wang 1998; Sampe and Xie 2010); however, a comprehensive and dynamically consistent interpretation of how this comes about is still lacking. Sampe and Xie (2010) suggest that the westerlies advect warm air downstream that then rises due to adiabatic uplift, thus providing a favorable environment for convection; the uplift is further intensified from the resulting latent heat release during

condensation. They also highlight the role of the westerlies in anchoring the mei-yu rainfall band via steering the weather disturbances along the jet. Chen and Bordoni (2014) confirm that the westerly jet induces low-level downstream convergence through providing horizontal advection of dry enthalpy, and argue that the meridional stationary eddy activity is crucial in sustaining the mei-yu front via transporting the mean temperature meridionally.

Paleoclimate reconstructions suggest that the intensity of the EASM varied considerably during the late Quaternary. Oxygen isotope records ($\delta^{18}O_p$) from Chinese caves suggest that the EASM during the Holocene changes in pace with orbital forcing on the precessional scales; that is, stronger Northern Hemisphere summer insolation induces enhanced EASM in the early to mid-Holocene (Wang et al. 2001, 2008). Based on the “amount effect” (Dansgaard 1964), this interpretation views the values of $\delta^{18}O_p$ recorded in the caves as a measure of EASM intensity (Wang et al. 2005). In agreement with the paleoproxy records, climate model simulations also suggest an intensified EASM during the mid-Holocene (e.g., Zheng et al. 2013). For example, the PMIP3 models median suggests that the summer precipitation over eastern China increases by 6.57% on average in the mid-Holocene simulations (Zheng et al. 2013).

Given that today’s EASM seasonal evolution is nontrivial, describing the early to mid- Holocene EASM as simply “more intense” is clearly incomplete. A recent modeling study (Shi 2016) argues for changes to the monsoon duration in the orbital-scale variability of EASM. Their results suggest that, under interglacial conditions, the length of rainy season over northern East Asia (33°–40°N, 105°–130°E) is longer for precession maxima (weaker boreal summer insolation) than for precession minima (stronger boreal summer insolation). Chiang et al. (2015) postulated that the defining characteristic of EASM changes in past climates is in the timing and duration of the EASM seasonal stages, rather than intensity. They furthermore invoke the dynamical link between the westerlies and the seasonal transition: their so-called jet transition hypothesis argues that the altered timing in the meridional migration of the westerlies relative to Tibet led to changes in the seasonal transition of the EASM in the past climate. They argue that the seasonality perspective can more consistently explain the varieties of existing proxy evidences of the East Asian paleoclimate changes, including speleothem, dust, and pollen records.

Following Chiang et al. (2015), this study explores orbitally induced EASM changes across the Holocene from the viewpoints of seasonality and the westerly jet. We simulate the orbitally induced Holocene changes to the EASM using “time snapshot” simulations of an atmospheric general circulation model (coupled to a slab ocean) that simulates the present-day EASM seasonal stages with fidelity. A novel feature of our analysis will be the use of “self-organizing maps” (SOMs) to objectively identify the spatial

pattern and timing of the EASM seasonal stages from the model rainfall simulations. We analyze the simulations to address two questions: 1) How does the timing, duration, and seasonal transition of the EASM change across the Holocene? 2) What factors are these changes in seasonality attributable to? For the first question, we show that orbitally driven EASM of the early to mid-Holocene is characterized by an advanced rainfall seasonality, with earlier mei-yu onset and an earlier transition from mei-yu to midsummer rainfall; this results in a shortened mei-yu rainfall stage and prolonged midsummer rainfall stage. For the second question, we show that the advanced seasonality is attributable to an earlier northward shift of the East Asian westerlies in the early to mid-Holocene compared to the present.

The study proceeds as follows. Section 2 describes the data, experiments, and the self-organizing maps. Section 3 presents the identification of the EASM seasonal stages from the SOMs. Section 4 presents our analysis of the simulated East Asian summer climates at various snapshots across the Holocene. Section 5 discusses the dynamical linkage between the westerlies and the seasonality of the EASM. Section 6 compares our results against two key paleoproxy observations of the Holocene East Asian climate, namely, the "asynchronous Holocene optimum" interpretation (An et al. 2000) and the dust proxy record, and shows that our seasonality interpretation is consistent with these observations. Conclusions and discussion are given in section 7.

2. Data, experiments, and method

a. Data

We use the APHRODITE rain gauge data (Yatagai et al. 2009) for the self-organizing maps (SOMs) analysis of the EASM rainfall patterns. APHRODITE data are also used to present the seasonal transitions of today's EASM (Fig. 1). The APHRO_MA_025deg_V1003R1 product covers 57 years (1951–2007) of daily precipitation on 0.25° × 0.25° grid within 15°S–55°N, 60°–150°E. This product has better quality control, incorporates more data, and has had bugs corrected when compared with the previous version APHRO_MA_V0902 (Yatagai et al. 2009). The gridded data only include rainfall values over land and are generated by interpolating rain gauge observations obtained from meteorological and hydrological stations over the region. The uncertainties of the APHRODITE lie in the discrepancies in the ending time for 24-h precipitation accumulation between countries, and the fact that the rain gauge network changes in region and time (Yatagai et al. 2012). Han and Zhou (2012) compared the APHRO_MA_025deg_V1003R1 product with daily precipitation obtained from 559 rain gauges with rigorous quality control in contiguous China. Compared with the station data, APHRODITE presents bias in both rainfall intensity and frequency; on the other hand, APHRODITE is able to precisely capture the seasonal transition of the rain belt and the long-term trend of precipitation amount over China (Han and Zhou 2012).

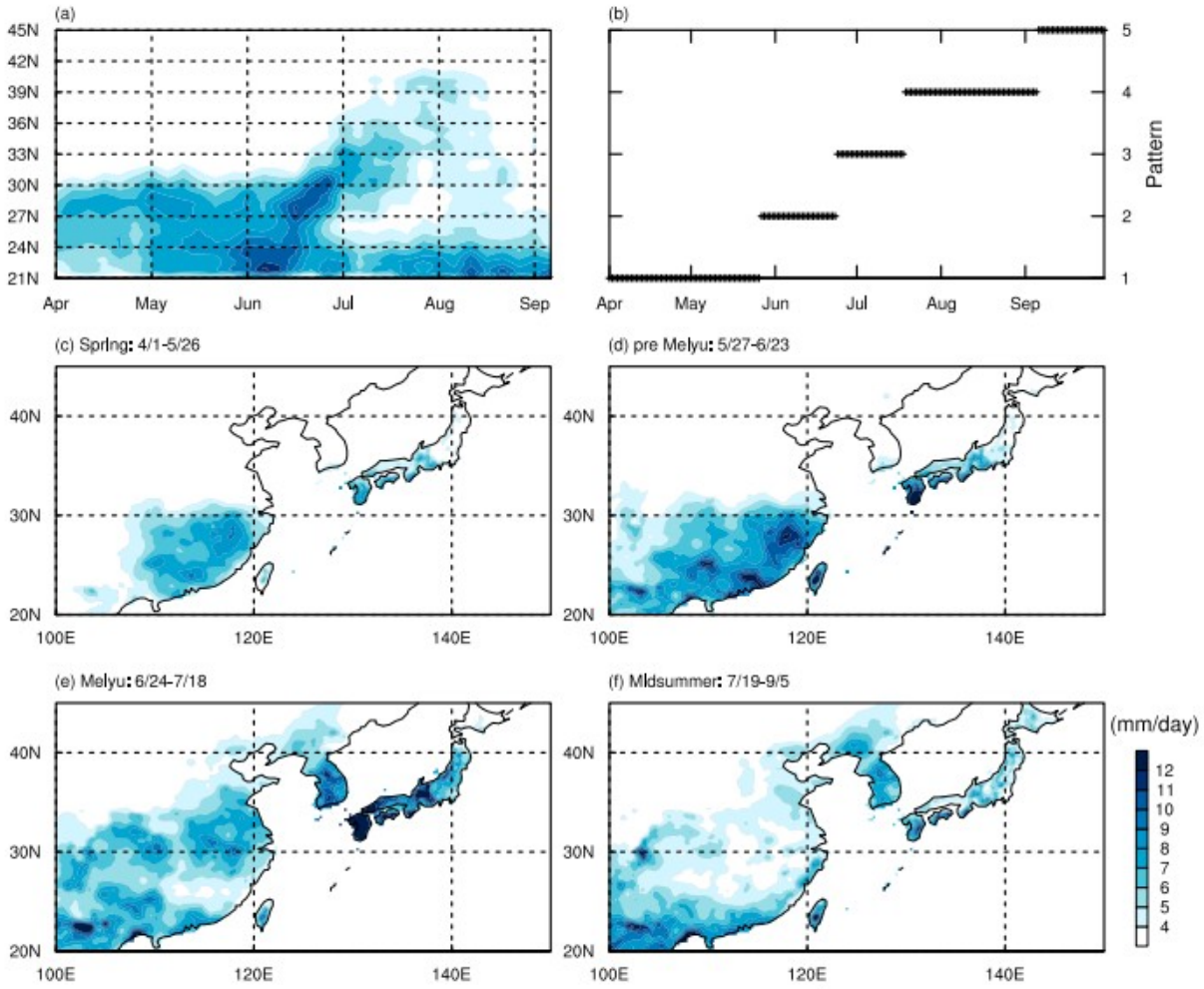

FIG. 1. Climatology of the 1951–2007 APHRODITE daily precipitation rate (unit: mm day^{-1}) over East Asia. (a) Hovmöller diagram of precipitation rate averaged from 110° to 120°E. Also shown are the (b) temporal and (c)–(f) spatial patterns of rainfall based on the SOMs analysis of the APHRODITE dataset: pattern 1 denotes the spring persistent rainfall (1 Apr–26 May) in (c), pattern 2 denotes the pre-mei-yu (27 May–23 Jun) in (d), pattern 3 denotes the mei-yu (24 Jun–18 Jul) in (e), and pattern 4 denotes the midsummer (19 Jul–5 Sep) in (f).

b. Experiments

Seven sets of numerical experiments are conducted using the E_1850_CAM5 component set from the National Center for Atmospheric Research's (NCAR) Community Earth System Model (CESM) version 1.2.2 (Hurrell et al. 2013), which includes the coupler, active atmosphere, land, and ice components, and a static slab ocean. The atmospheric component of the CESM1 is the Community Atmosphere Model version 5 (CAM5) at 0.9° × 1.25° horizontal resolution and 30 layers of vertical resolution. The ocean heat transport convergence (i.e., the "Q flux") from a CESM1 preindustrial fully coupled run (available on the Yellowstone high-performance IBM cluster at NCAR) is prescribed to the slab ocean model to achieve a simulated sea surface temperature close to the preindustrial.

We apply the CAM5 to seven time periods—9000 years before present (9 ka hereafter), 7.5, 6, 4.5, 3, 1.5 ka, and preindustrial (PI)—and the insolation at

the top of atmosphere is prescribed for each time segment by specifying the corresponding year, and the model computes the corresponding eccentricity, obliquity, and precession (Berger et al. 1993). The GHG concentrations in our PI simulation are set to default values as in the CESM preindustrial configuration (i.e., CO_2 is 284.7 ppm, CH_4 is 791.6 ppb, and N_2O is 275.68 ppb). Following the Paleoclimate Modeling Intercomparison Project phase 3 (PMIP3) protocol (Braconnot et al. 2012), we prescribe the atmospheric content of CH_4 at 650 ppb in the 9-, 7.5-, 6-, 4.5-, 3-, and 1.5-ka experiments, while keeping CO_2 and N_2O fixed at their values for the PI. Land surface type is kept to the same as for the preindustrial control. Each experiment is integrated for 60 years, with the first 30 years treated as spinup; the climatology derived over the last 30 years is used for the analysis presented. We use the Student's t test to present the statistical significance of the difference in the climatological means, with the null hypothesis that the anomaly is not significantly different from zero. To this end, we make the assumption that the samples used in calculating the statistical significance at each grid point are drawn from a Gaussian distribution (i.e., normally distributed) and independent of each other.

c. Self-organizing maps

Our problem requires accurate and objective identification of the seasonal EASM rainfall stages. Given that they exhibit unique spatial characteristics, and the transitions between them are abrupt, a cluster analysis is ideally suited for this analysis. The SOMs method is a neural network–based cluster analysis that classifies a high-dimensional dataset into representative patterns (Kohonen 2001; Kohonen et al. 1996). It uses a neighborhood function to topologically order the high-dimensional input, grouping similar clusters together. The SOMs method has advantages over the empirical orthogonal function (EOF) technique in extracting nonlinear features (Iskandar 2009; Liu et al. 2006). In addition, the SOMs method distinguishes itself from other clustering analyses, such as the k-means method (Lin and Chen 2006) and Ward's method (Bao and Wallace 2015; Solidoro et al. 2007), via extracting more distinctive and more robust representative patterns. Unlike EOFs, however, there is no straightforward way to reconstruct the dataset from the patterns derived from the SOMs (Liu et al. 2006). The SOMs method has been used successfully to characterize patterns of climate variations such as El Niño–Southern Oscillation (Johnson 2013) and the Northern and Southern Hemisphere teleconnection patterns (Chang and Johnson 2015; Johnson et al. 2008). This approach was first applied in the Asian monsoon by Chattopadhyay et al. (2008) for the intraseasonal oscillation of the Indian summer monsoon and has been applied to demonstrate the intraseasonal modes of the East Asian–western North Pacific summer monsoon (Chu et al. 2012). In this study, we use the SOMs to identify the distinct phases of rainfall during the seasonal transitions of the EASM.

We first applied the SOMs to the APHRODITE daily climatology during 1951–2007. We chose 20°–45°N, 110°–140°E (Wang and LinHo 2002) as the domain for the EASM. Only data over land were used and each grid box was weighted by the square root of the cosine of latitude. We took the 5-day running mean of this latitude-weighted daily climatology and chose the summer half year (April–September) for the SOMs analysis.
Following Johnson (2013), we use the Epanechicov neighborhood function and the batch training algorithm in the present analysis. We did a statistical distinguishability test as in Johnson (2013) and specified the number of nodes (K) to be 5 to match the number of expected rainfall patterns.

To test whether our simulations capture the seasonal stages of the EASM in a realistic way, we proceed to repeat the SOMs analysis of the APHRODITE dataset in the PI simulation. Note that we took the 7-day running mean of the daily rainfall climatology for the SOMs analysis in the PI simulation. We then match the 30-yr daily rainfall climatology from the remaining simulations to the SOMs patterns of the PI run. Each daily rainfall field is assigned to a best-matching SOMs pattern based on the minimum Euclidean distance.

For further specifics of the SOMs technique, the readers are referred to Johnson (2013) and the appendix of Johnson et al. (2008).

3. Identification of the EASM seasonal stages from SOMs analysis

In this section, we show that the SOMs analysis is able to objectively extract the seasonal stages of the EASM in observed precipitation data, and we furthermore show that the CAM5 is capable of simulating the EASM seasonal stages.

Figure 1a shows the latitude–time cross section of precipitation over eastern China (110°–120°E), reflecting the onset process of the EASM as summarized in Ding and Chan (2005): 1) Following the spring persistent rainfall (Wu et al. 2007), the pre-mei-yu season starts from the first 10-day period of May and features a steep rise in precipitation between 18° and 25°N. 2) The rain belt shifts to the valley of the Yangtze River in mid-June, the traditional Chinese mei-yu season. 3) From mid-July, the second jump of the rain belt brings more rainfall over northern and northeastern China, forming the midsummer rainfall season. 4) The southward retreat of the monsoon rain belt from the end of August to early September indicates the end of the EASM.

Largely in agreement with Ding and Chan (2005), SOMs analysis of the APHRODITE data (Figs. 1b–f) extracts the seasonal stages and transitions of the EASM accurately. Figure 1b presents the temporal rainfall patterns, here called “spring” (pattern 1), “pre-mei-yu” (pattern 2), “mei-yu” (pattern 3) and “midsummer” rainfall (pattern 4), during the seasonal transitions. Pattern 5 denotes the end of the EASM. Figures 1c–f present the spatial maps of the spring (Fig. 1c), pre-mei-yu (Fig. 1d), mei-yu (Fig. 1e), and midsummer (Fig. 1f) patterns based on the SOMs analysis. These results show that the

SOMs method is able to distinctly extract the seasonal stages of the EASM, including both the spatial pattern and the timing and duration of each rainfall stage. We note that the onset timing of the pre-mei-yu and mei-yu stages from the APHRODITE SOMs is slightly delayed compared to Ding and Chan (2005): instead of early May and mid-June as in Ding and Chan (2005), here the pre-mei-yu starts in late May and the mei-yu in late June in our SOMs analysis. This difference may be due to the fact that the precipitation data and the time range used in our SOMs analysis are different from those in Ding and Chan (2005).

We now show that CAM5 can reasonably simulate the seasonal stages of the EASM. First, the Hovmöller diagram of the precipitation over eastern China (110°–120°E) from the PI simulation (Fig. 2a) clearly captures the stepwise northward transition of the EASM rain belt, resembling today's rain gauge data (Fig. 1a). Second, by employing the SOMs method in the PI simulation, Figs. 2b–f suggest that the seasonality of the EASM simulated in CAM5 is largely consistent with that in the APHRODITE data (Figs. 1b–f). Besides the slight shift in the onset timing compared to the APHRODITE, the largest biases in the simulation come from the spatial pattern of each stage. For example, the position of the spring (Fig. 2c) and pre-mei-yu (Fig. 2d) patterns are northward shifted compared to APHRODITE (Figs. 1c,d). Although bias does exist, the CAM5 clearly simulates the seasonal transitions of the EASM with reasonable fidelity.

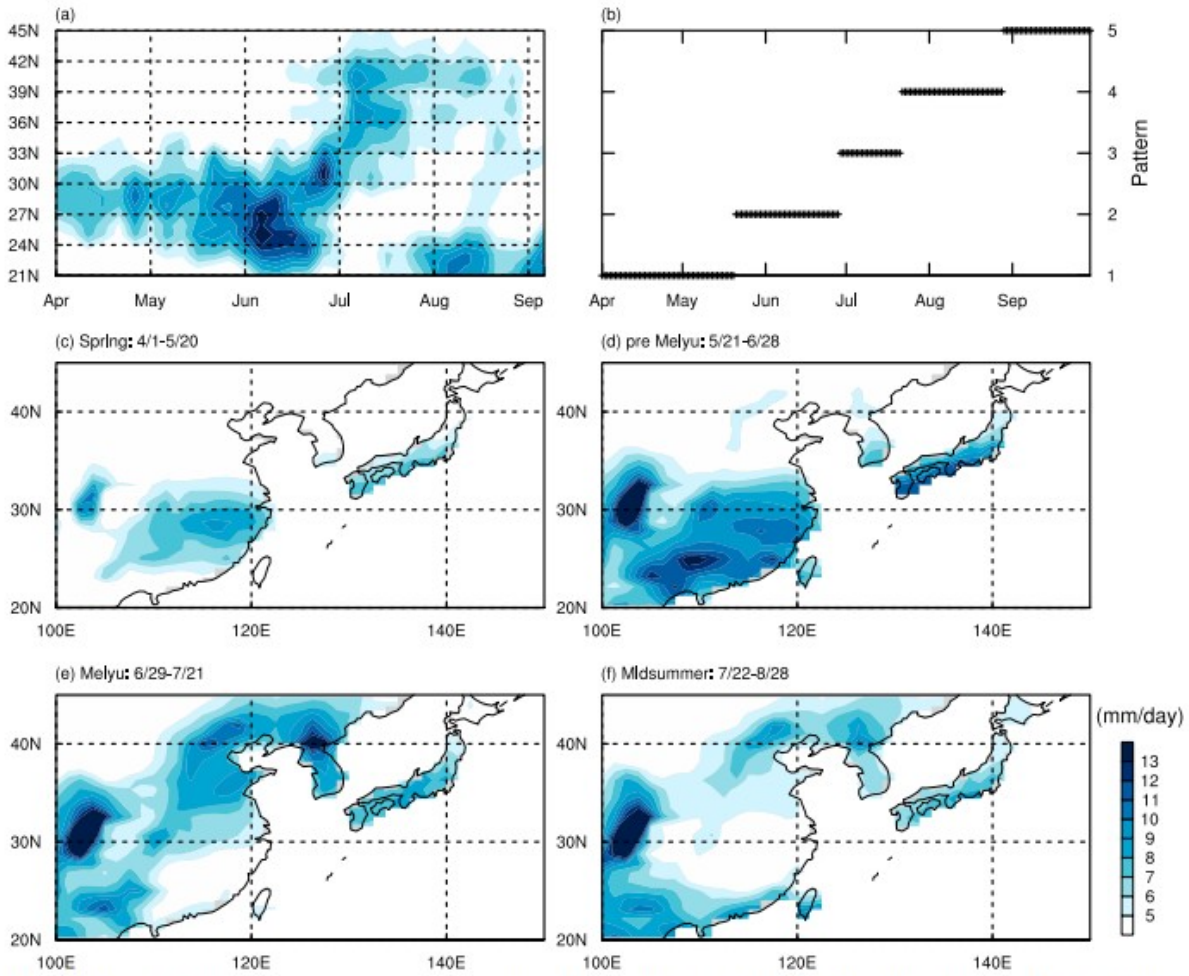

FIG. 2. The East Asian summer monsoon from the preindustrial simulation in CAM5. (a) Hovmöller diagram of the precipitation averaged between 110° and 120°E. (b) The SOMs temporal patterns. (c)–(f) The SOMs spatial patterns averaged over the periods indicated, respectively: pattern 1 (spring; 1 April–20 May 20), pattern 2 (pre-mei-yu; 21 May–28 June), pattern 3 (mei-yu; 29 June–21 July), and pattern 4 (midsummer, 22 July–28 August).

In the next two sections, we will show our analysis of the simulated Holocene EASM in CAM5 on the basis of the SOMs method.

4. Changes to the EASM seasonality over the Holocene

The SOMs analysis provides an objective method to extract the seasonal stages of the EASM. In this section, we use this method on the Holocene simulations to show that the simulated EASM experiences gradually delayed seasonal transitions across the Holocene. We furthermore show that the meridional positioning of the westerlies shifts gradually southward across the Holocene, consistent with its hypothesized role in determining the timing of the EASM seasonal transitions.

a. General results

Table 1 and Fig. 3 (the visualization of Table 1) show the onset timing and length (on the average basis) of the mei-yu and midsummer derived from the SOMs analysis across the simulated Holocene. The onset of mei-yu and

midsummer delays gradually from the early to the late Holocene. For example, the onset of mei-yu in 9 ka, on 12 June, is two weeks earlier than that in PI, which is on 29 June. Similarly, the onset of midsummer in 9 ka, which is on 25 June, starts about one month earlier than that in PI. In addition, Table 1 shows that the early to mid-Holocene features shorter mei-yu duration and longer midsummer duration compared to the late Holocene. For instance, the duration of mei-yu in PI (23 days) is about twice as long as that in 9 ka (13 days), and the duration of midsummer in PI (38 days) is less than half of that in 9 ka (81 days).

TABLE 1. Statistics of mei-yu and midsummer rainfall in the Holocene simulations.

Simulation	Mei-yu onset	Mei-yu duration	Midsummer rainfall onset	Midsummer rainfall duration
PI	29 Jun	23 days	22 Jul	38 days
1.5 ka	25 Jun	25 days	20 Jul	54 days
3 ka	25 Jun	17 days	12 Jul	56 days
4.5 ka	24 Jun	15 days	9 Jul	63 days
6 ka	23 Jun	16 days	9 Jul	66 days
7.5 ka	19 Jun	9 days	28 Jun	79 days
9 ka	12 Jun	13 days	25 Jun	81 days

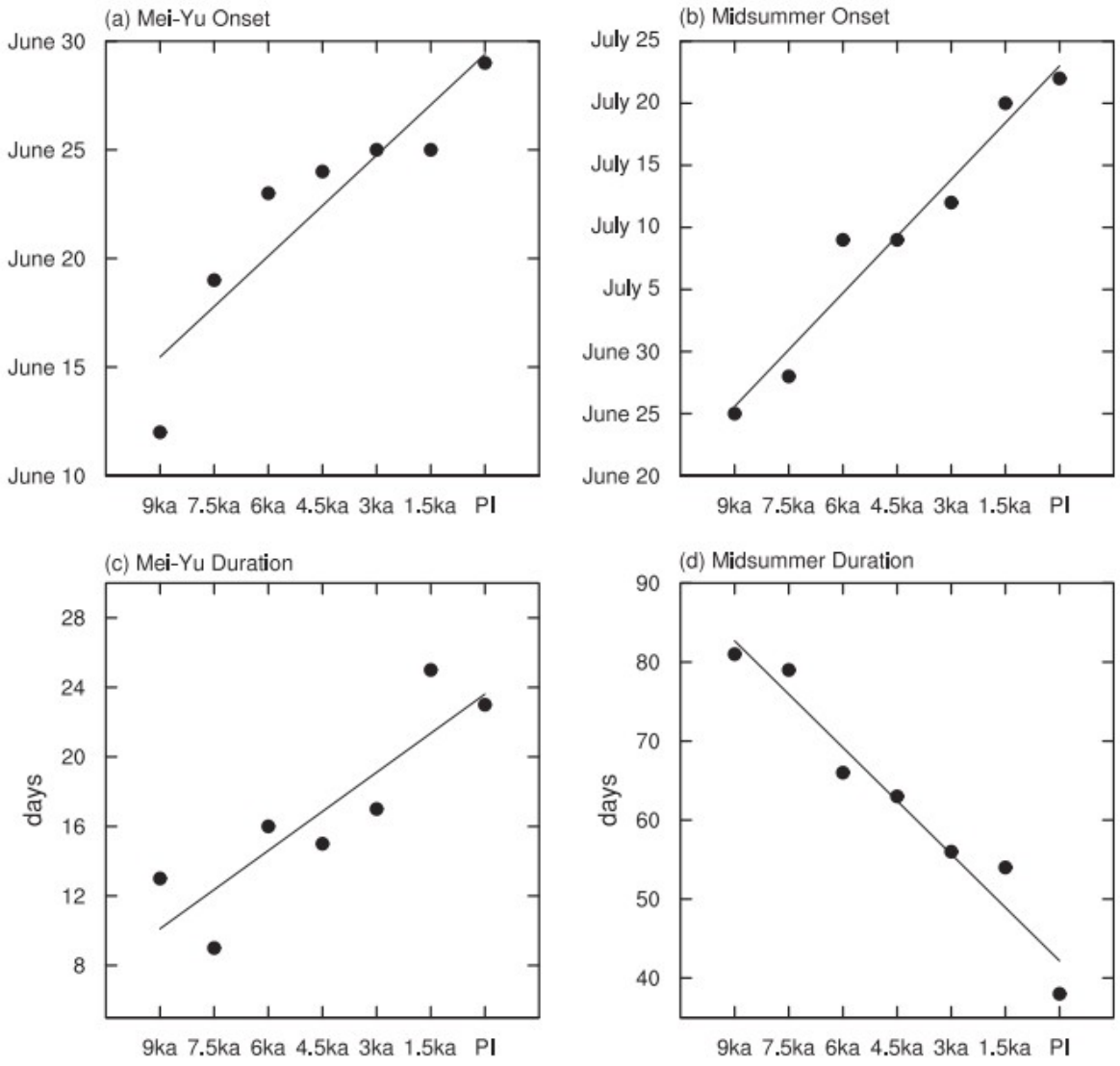

FIG. 3. (a),(b) Onset timing and (c),(d) duration of the mei-yu and midsummer rainfall patterns, respectively, across the Holocene. The result of PI is based on the SOMs analysis, and the results of the rest simulations are derived by matching to the SOMs patterns of PI. The solid lines indicate the best-fit linear least squares regression based on the results.

Figure 4 shows the temporal evolution of EASM seasonality in the 9-, 6-, 3-ka, and PI simulations, using a zonal average of the daily rainfall climatology over 110°–120°E. Consistent with Fig. 3, Fig. 4 depicts a gradual shift of timing in the total rainfall transition from 9 ka to PI, suggesting that the seasonal transition of the EASM occurs earlier in 9 and 6 ka relative to 3 ka and PI. The evolution becomes particularly notable when we separate the total precipitation into the large-scale precipitation (Figs. 4e–h) and convective precipitation (Figs. 4i–l). Large-scale precipitation is characteristic of the rainfall over southern China during the spring and pre-mei-yu (Figs. 4e–h), whereas convective precipitation dominates the mei-yu and midsummer rainfall seasons (Figs. 4i–l). The changes in the large-scale and

convective rainfall are consistent with our hypothesis that the spring and pre-mei-yu are shortened during the early to mid-Holocene, and that the onset of mei-yu and midsummer appears earlier. Compared to 3 ka and PI, the 9- and 6-ka experience shorter mei-yu duration and longer midsummer duration. The common interpretation of the early Holocene EASM is that it is more “intense” (e.g., Wang et al. 2008). It begs the question of how this relates to our finding that the seasonal transitions occur earlier. To evaluate summer monsoon “intensity” in the simulations, the fourth column in Fig. 4 shows the averaged total precipitation (110°–120°E) over the entire summer rainfall period including June, July, August, and September. The notable aspect of this seasonally averaged picture is that whereas the rainfall over northern China (north of 36°N) is stronger in the early to mid-Holocene, the rainfall over southern China (south of 36°N) is actually weaker, in particular during the 6-ka period. Thus, describing the early to mid-Holocene EASM as being more intense clearly does not capture this regional heterogeneity in the rainfall response. Rather, the seasonality perspective—a shorter mei-yu and longer midsummer stage—provides a more accurate picture of the early to mid-Holocene rainfall changes over eastern China.

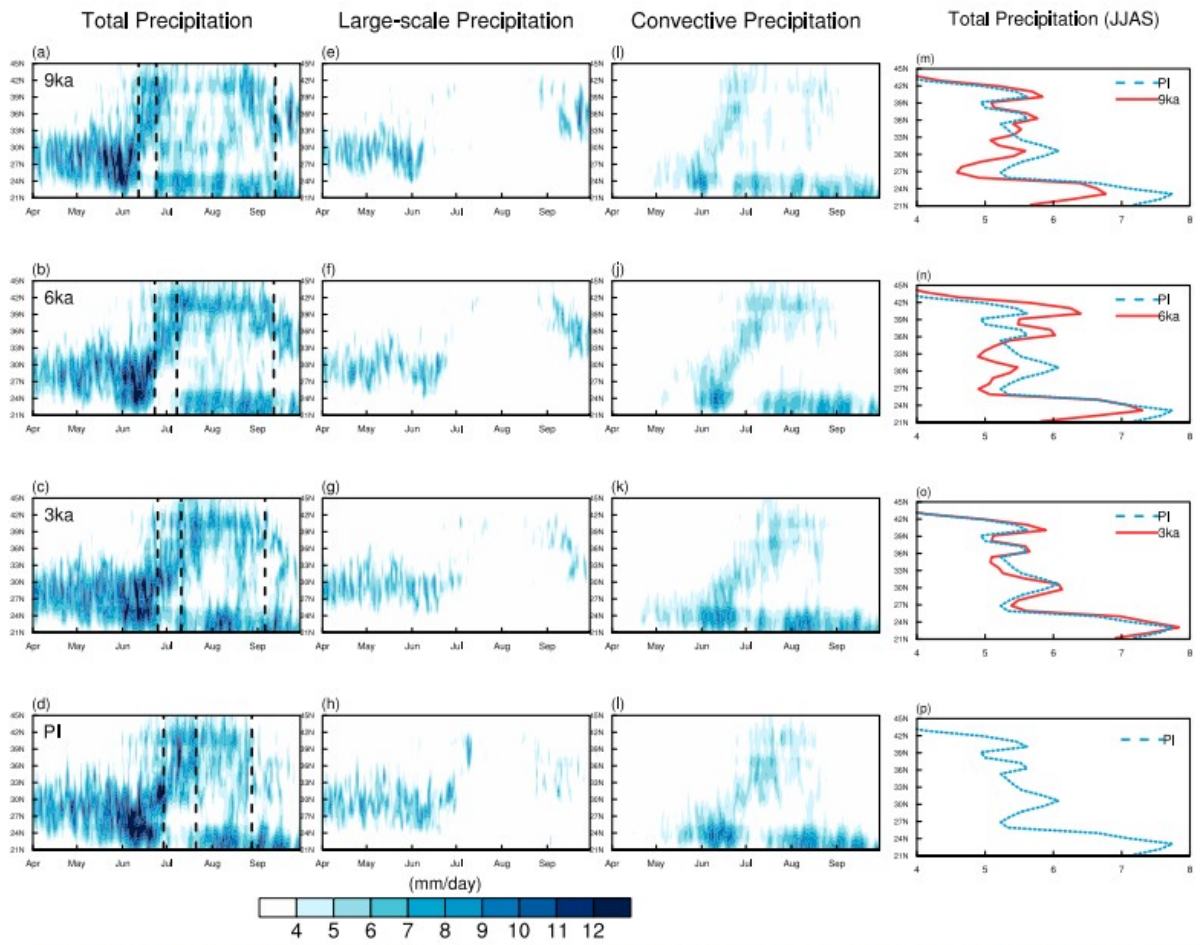

FIG. 4. Seasonal transition of (a)–(d) total, (e)–(h) large-scale, and (i)–(l) convective precipitation rate, and (m)–(p) the averaged total precipitation (110°–120°E) in June–September, in (from top to bottom) the 9-, 6-, 3-ka, and PI simulations, averaging from 110° to 120°E. The *x* axis indicates the strength of the rainfall. The blue dashed line denotes the results from PI, while the red solid lines denote the results from the 9-, 6-, and 3-ka runs. The unit is mm day^{-1}.

Unlike the 6 and 9 ka, the 3 ka does not show evident advance in the timing of the seasonal transitions compared to PI. This may be attributable to the nature of the insolation changes between those periods. For 9 and 6 ka, the increased summer insolation anomalies occur at the beginning of April for 9 ka and May for 6 ka (Fig. 5), which is sufficiently early to affect the transitions to the mei-yu and midsummer regimes. For 3 ka, however, the positive insolation anomalies only start in June.

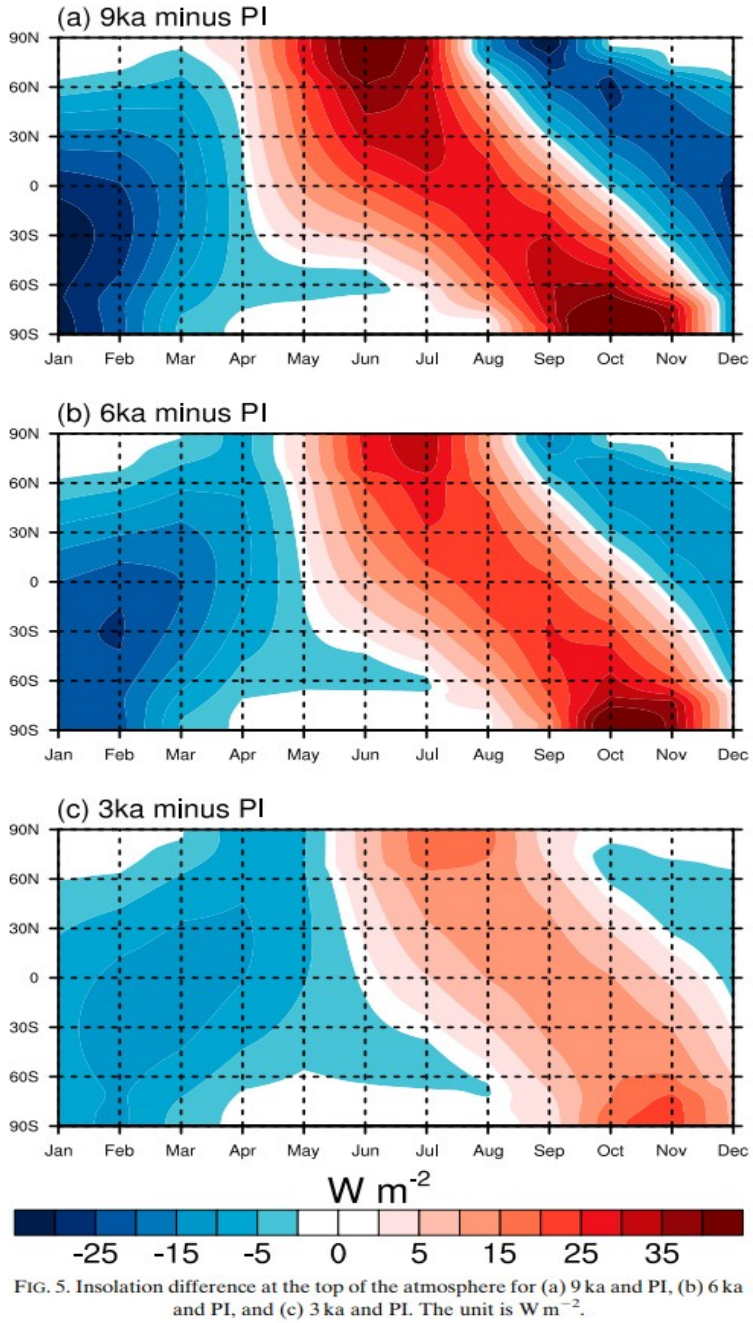

FIG. 5. Insolation difference at the top of the atmosphere for (a) 9 ka and PI, (b) 6 ka and PI, and (c) 3 ka and PI. The unit is W m^{-2}.

To further elucidate the difference of the EASM between the early to mid-Holocene and the late Holocene, we will subsequently focus our analysis to the 6 ka compared against the PI. Based on the timing of the rainfall seasonal transitions in PI (Table 1), we define 29 June–21 July as the PI mei-yu and 22 July–28 August as the PI midsummer rainfall season. Similarly, we define 23 June–8 July as the 6-ka mei-yu season and 9 July–12 September as the 6-ka midsummer rainfall season.

b. Changes to the EASM frontal position and moisture transports and convergence

To confirm our interpretation (thus far based only on rainfall changes) that the onset of the mei-yu and midsummer periods in 6 ka appears earlier, we examine the mei-yu frontal position and associated moisture transports. The mei-yu front is characterized by a steep meridional gradient in equivalent potential temperature (θ_e) across northern China (Ninomiya 1984; Tomita et al. 2011). Here we use the maximum in the meridional gradient of moist static energy (MSE) $[-\partial(\mathrm{MSE})/\partial y]$ to approximately indicate this position (Fig. 6). The MSE is given by

$$\mathrm{MSE} = C_p T + L_v q + gz,$$

where C_p is the specific heat at constant pressure ($1004\,\mathrm{J\,kg^{-1}\,K^{-1}}$), T is the temperature (K), g is the gravitational constant (9.81 m s^{-2}), z is the geopotential height (m), L_v is the latent heat of vaporization ($2.5 \times 10^6\,\mathrm{J\,kg^{-1}}$), and q is the specific humidity (kg kg^{-1}). In the PI mei-yu phase (29 June–21 July), the front is located around 30°–40°N (Fig. 6b). During 29 June–1 July in 6 ka, the front is located around 40°–50°N (Fig. 6a). Also, there is a decrease in the MSE gradient in 30°–40°N and an increase to the north of 45°N (Fig. 6c), suggesting an earlier northward shift of the frontal systems in 6 ka and therefore earlier mei-yu onset. In the PI midsummer rainfall season (22 July–28 August), the front is weakened and moves to northern China (Fig. 6e); the front during the same time at 6 ka shifts farther poleward (Fig. 6f), suggesting the early termination of mei-yu season and early onset of the midsummer rainfall. The moisture flux at 850 mb is shown in Fig. 7. The simulations demonstrate that during 6 ka there is stronger low-level monsoonal flow delivering more moisture to central to northern China in the PI mei-yu phase (Fig. 7c) and to northern China in the PI midsummer rainfall phase (Fig. 7f). Together, the northward frontal shift and increased low-level moisture transport suggest an earlier seasonal transition from pre-mei-yu to mei-yu and from mei-yu to midsummer rainfall in 6 ka.

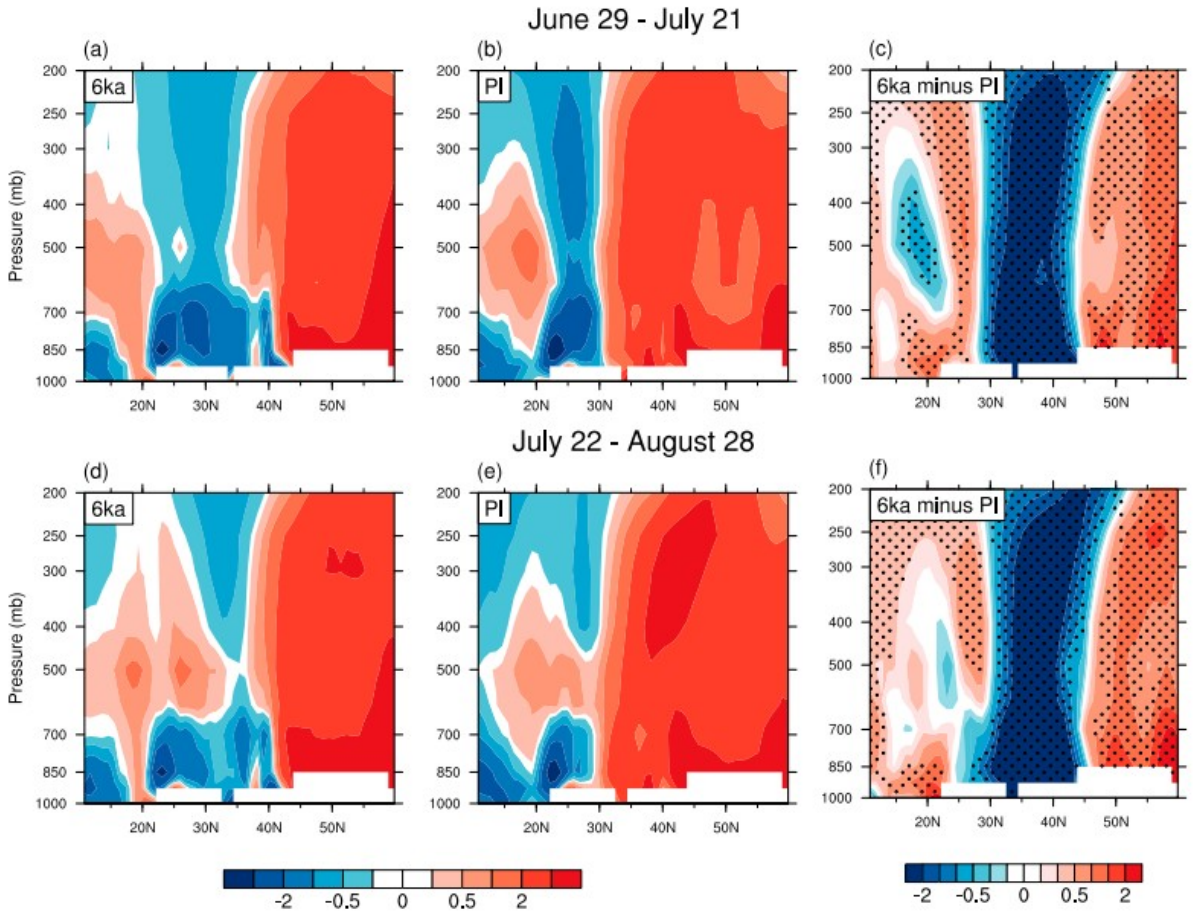

FIG. 6. Pressure–latitude (10°–60°N) cross section of the meridional gradient of MSE $[-\partial(\mathrm{MSE})/\partial y]$ averaged over 110°–120°E, for (top) 29 Jun–21 Jul (i.e., the mei-yu season in PI) and (bottom) 22 Jul–28 Aug (i.e., the midsummer season in PI), for (left) 6 ka, (middle) PI, and (right) 6 ka minus PI. The stippled areas indicate that the difference is statistically significant at the confidence level of 90%. The unit is $3 \times 10^{-6}\,\mathrm{kJ^2\,kg^{-1}\,m^{-1}}$.

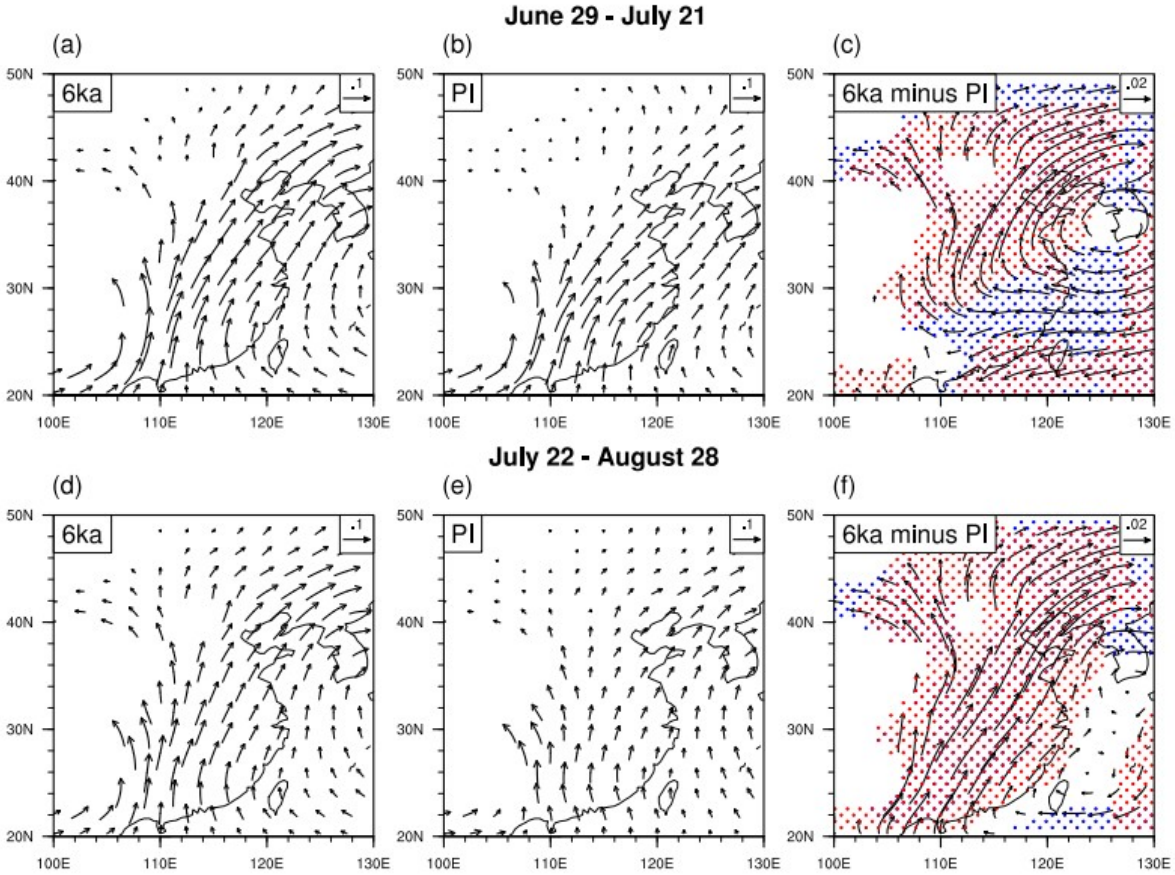

FIG. 7. Moisture flux (vectors) at 850 mb for (top) 29 Jun–21 Jul (i.e., the mei-yu season in PI) and (bottom) 22 Jul–28 Aug (i.e., the midsummer season in PI), for (left) 6 ka, (middle) PI, and (right) 6 ka minus PI. The blue (red) dots indicate that the difference in zonal moisture flux ($\mathbf{u}q$) [meridional moisture flux ($\boldsymbol{v}q$)] is statistically significant at the confidence level of 90%. [The unit is $10^3\,\mathrm{g\,kg^{-2}\,m^{-1}\,s^{-1}}$, and the reference vector is $0.1\times10^3\,\mathrm{g\,kg^{-2}\,m^{-1}\,s^{-1}}$ in (a),(b),(d), and (e) and $0.02\times10^3\,\mathrm{g\,kg^{-2}\,m^{-1}\,s^{-1}}$ in (c) and (f).]

Our interpretation is further corroborated by the changes in the relative vorticity ($\zeta = \partial v/\partial x - \partial u/\partial y$) and moisture convergence ($-\nabla\cdot(\boldsymbol{v}q) = -[\partial(uq)/\partial x + \partial(vq)/\partial y]$) at 850 mb (Fig. 8). As shown in Chen et al. (1998), high cyclonic vorticity is associated with convective rainstorms along the mei-yu front. The ascending motion generated by strong latent heat release stretches the local troposphere air mass vertically and creates the low-level convergence, which combines the low-level horizontal wind shear associated with the low-level jet, to force the rapid spinup of low-level vorticity [see Fig. 20 of Chen et al. (1998)]. Our simulation suggests that the high cyclonic vorticity zone is displaced northward from PI to 6 ka, which can be seen in both the periods of the PI mei-yu (Fig. 8c) and PI midsummer rainfall seasons (Fig. 8f). In addition, the 6-ka moisture convergence is enhanced to the north of 40°N (Figs. 8c,f), which likely results from the combined effect of the ascending motion along the northward-displaced frontal systems (Figs. 6c,f) as well as the enhanced poleward moisture supplies (Figs. 7c,f).

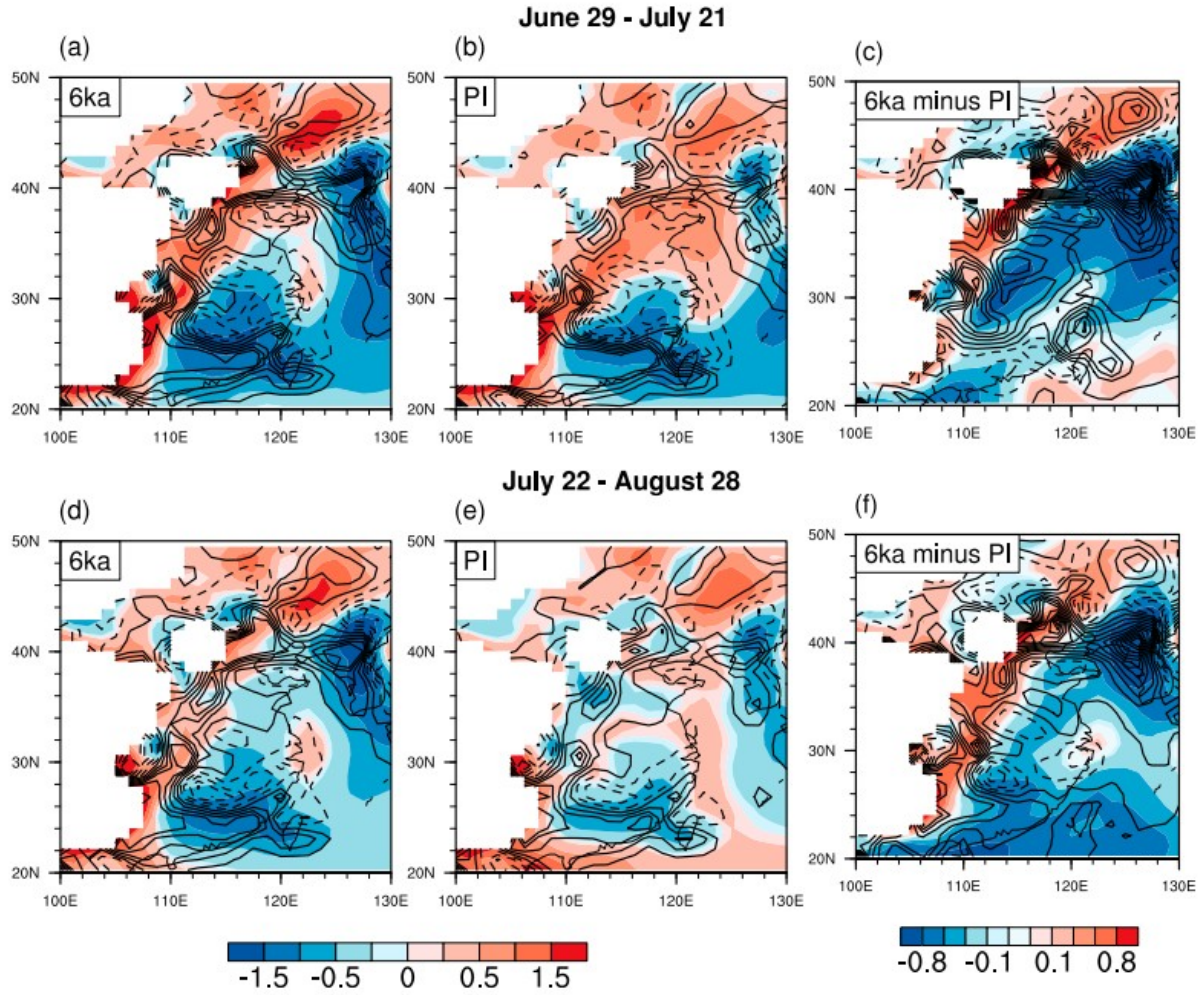

FIG. 8. Relative vorticity (shading, the unit is $10^{-5}\,s^{-1}$) and moisture divergence [contour, contour interval $0.25\times10^{-7}\,s^{-1}$ for (a),(b),(d), and (e), $0.1\times10^{-7}\,s^{-1}$ for (c) and (f); negative values are in dashed lines] at 850 mb. Results are shown for (top) 29 Jun–21 Jul (i.e., the mei-yu in PI) and (bottom) 22 Jul–28 Aug (i.e., the midsummer in PI) for (left) 6 ka, (middle) PI, and (right) 6 ka minus PI. Warm (cold) color indicates cyclonic (anticyclonic) vorticity. The solid (dashed) lines indicate moisture divergence (convergence).

c. Is the PI mei-yu (midsummer) the same as the 6-ka mei-yu (midsummer)?

We have shown that the EASM seasonal stages occur with different timings in the Holocene simulations. A further question we can ask is this: If we compare the climate fields associated with the PI mei-yu (or midsummer) stage with those from the 6 ka (in other words, allowing for the difference in timing and duration), are the fields similar, or not? In other words, does the PI mei-yu (midsummer) dynamically resemble the 6-ka mei-yu (midsummer)?

The answer appears to be no, at least quantitatively. Figure 9 compares the frontal position and the moisture transport between PI mei-yu and 6-ka mei-yu and between PI midsummer and 6-ka midsummer. The fronts and the moisture flux penetration during mei-yu (midsummer) in 6 ka reach more northward locations compared to the PI, indicating more northward positioning of the rain belt in 6 ka. Similar analyses for the westerlies (Figs.

10b,d) suggest more northward positioning of the westerlies relative to the Tibetan Plateau in 6-ka mei-yu and midsummer.

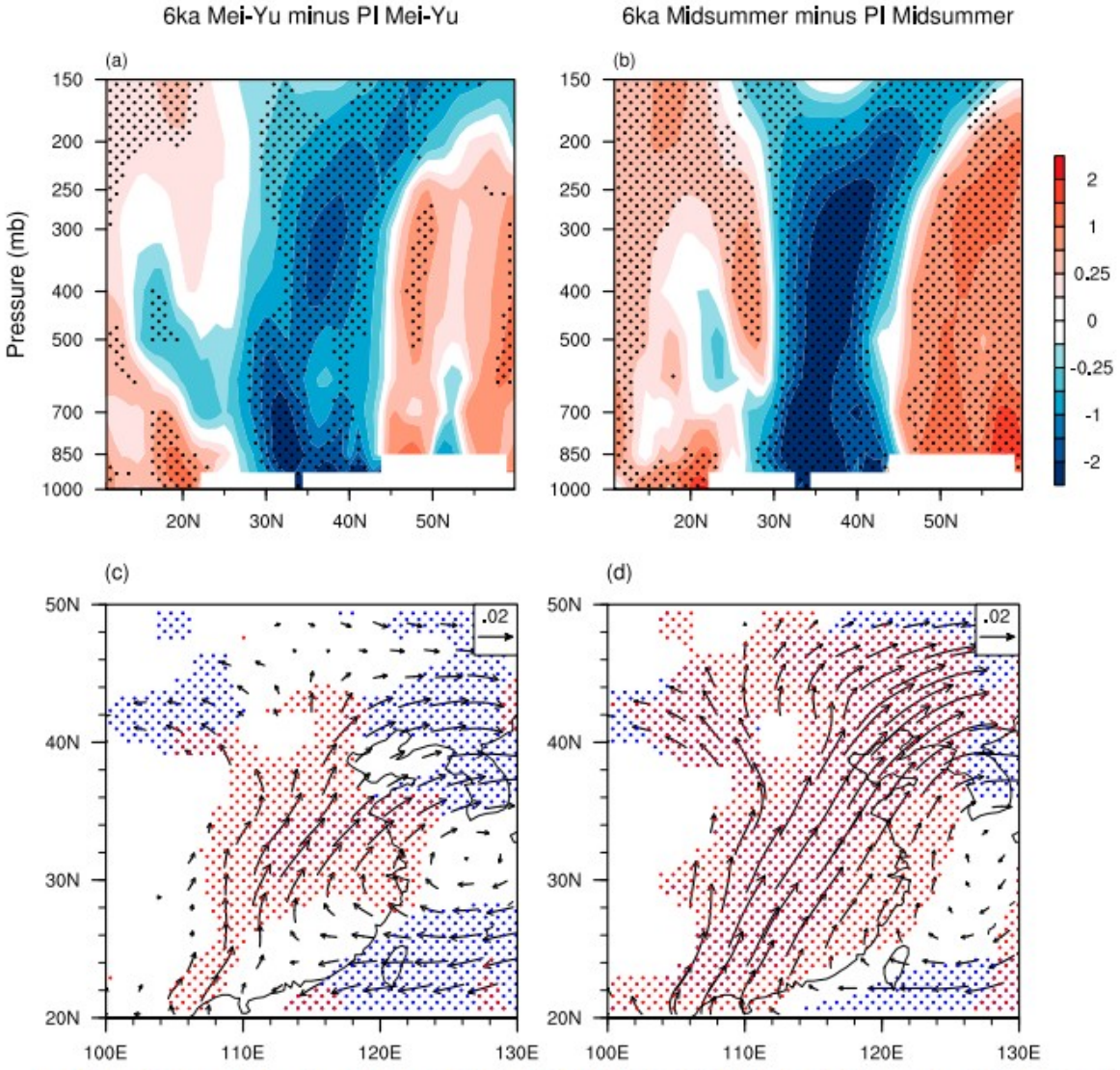

FIG. 9. (top) The meridional gradient of MSE $[-\partial(\mathrm{MSE})/\partial y]$ (110°–120°E) for (a) 6-ka mei-yu (23 Jun–8 Jul) minus PI mei-yu (29 Jun–21 July and (b) 6-ka midsummer (9 Jul–12 Sep) minus PI midsummer (22 Jul–28 Aug). The stippled areas indicate that the difference is statistically significant at the confidence level of 90%. The unit is $3 \times 10^{-6}\,\mathrm{kJ^2\,kg^{-1}\,m^{-1}}$. (bottom) The moisture flux (850 mb) for (c) 6-ka mei-yu minus PI mei-yu and (d) 6-ka midsummer minus PI midsummer. The blue (red) dots indicate that the difference in zonal moisture flux ($\mathbf{u}q$) [meridional moisture flux ($\boldsymbol{\nu}$q)] is statistically significant at the confidence level of 90%. The unit is $10^3\,\mathrm{g\,kg^{-2}\,m^{-1}\,s^{-1}}$, and the reference vector $0.02 \times 10^3\,\mathrm{g\,kg^{-2}\,m^{-1}\,s^{-1}}$.

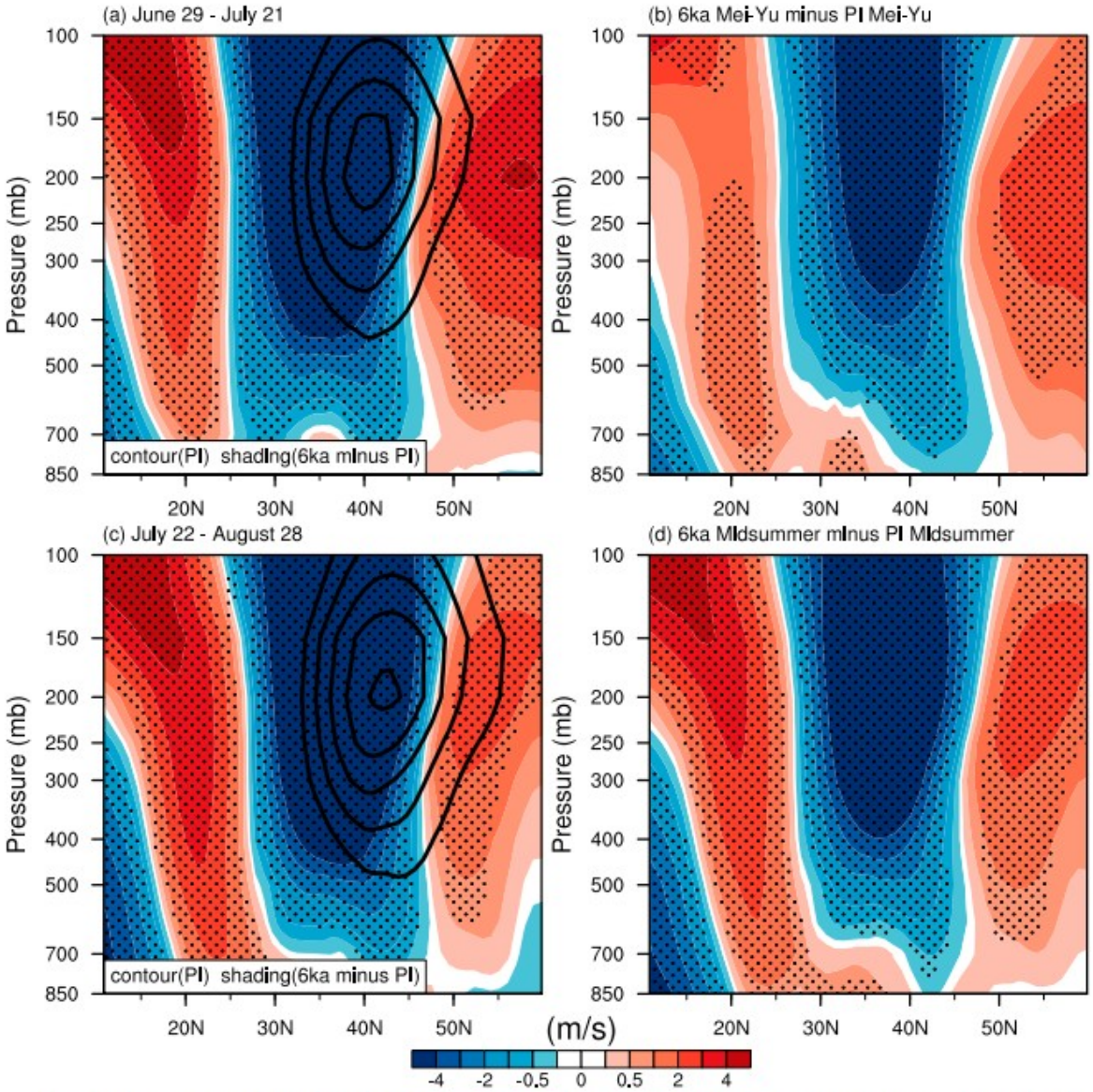

FIG. 10. (left) The zonal wind (80°–120°E) during (a) 29 Jun–21 Jul and (c) 22 Jul–28 Aug (contour: PI; shading: 6 ka minus PI). (right) The zonal wind (80°–120°E) for (b) the 6-ka mei-yu season (23 Jun–8 Jul) minus PI mei-yu season (29 Jun–21 Jul), and (d) the 6-ka midsummer season (9 Jul–12 Sep) minus PI midsummer season (22 Jul–8 Aug). The stippled areas indicate that the differences of zonal wind are statistically significant at the confidence level of 95%.

This suggests that the 6-ka mei-yu is more intense than the PI mei-yu; the same appears to be the case if the midsummer stages are compared. The reason for this appears to again be tied to the westerlies, namely that a more northward positioned westerly jet in 6 ka relative to the PI allows for more northward-penetrating fronts and moisture flux to occur. However, dynamically, the PI and 6-ka mei-yu (or midsummer) qualitatively resemble each other.

5. Role of the westerlies in the EASM changes

Chiang et al. (2015) hypothesized that earlier seasonal transitions in the EASM correspond to earlier northward transitions of the westerlies relative to the Tibetan Plateau. This view appears to be supported in our 6-ka Holocene simulation (Figs. 10a,c). The strengthened westerlies to the north of the PI jet core and weakened westerlies to the south of the PI jet core indicate an earlier northward displacement of the westerly jet in 6 ka during the PI mei-yu phase (Fig. 10a) and the PI midsummer phase (Fig. 10c) (note that the westerly anomalies to the south of 30°N in Figs. 10a and 10c are due to the weaker easterlies over southern China in 6 ka). In the following two subsections, we explore mechanisms linking the seasonality of the EASM to the East Asian westerlies.

a. The dynamical linkage between the westerlies and the EASM

To understand the origins of the earlier northward migration of the westerlies, we examine changes to the meridional temperature gradient induced by the insolation changes. Figures 11a–c show the Hovmöller diagram of the meridional temperature gradient ($-\partial T/\partial y$) at 200 mb over East Asia (80°–120°E). Compared to the PI, the meridional temperature gradient in 6 ka is weaker, and the northward movement of the maximum gradient belt in 6 ka is faster from May to August. Also, the position of the positive temperature gradient is farther north in 6 ka during July and August (see the positive anomaly in Fig. 11c). Consistent with the changes in the meridional temperature gradient, the 6-ka features weakened and northward-shifted westerlies, as shown in Figs. 11d–f.

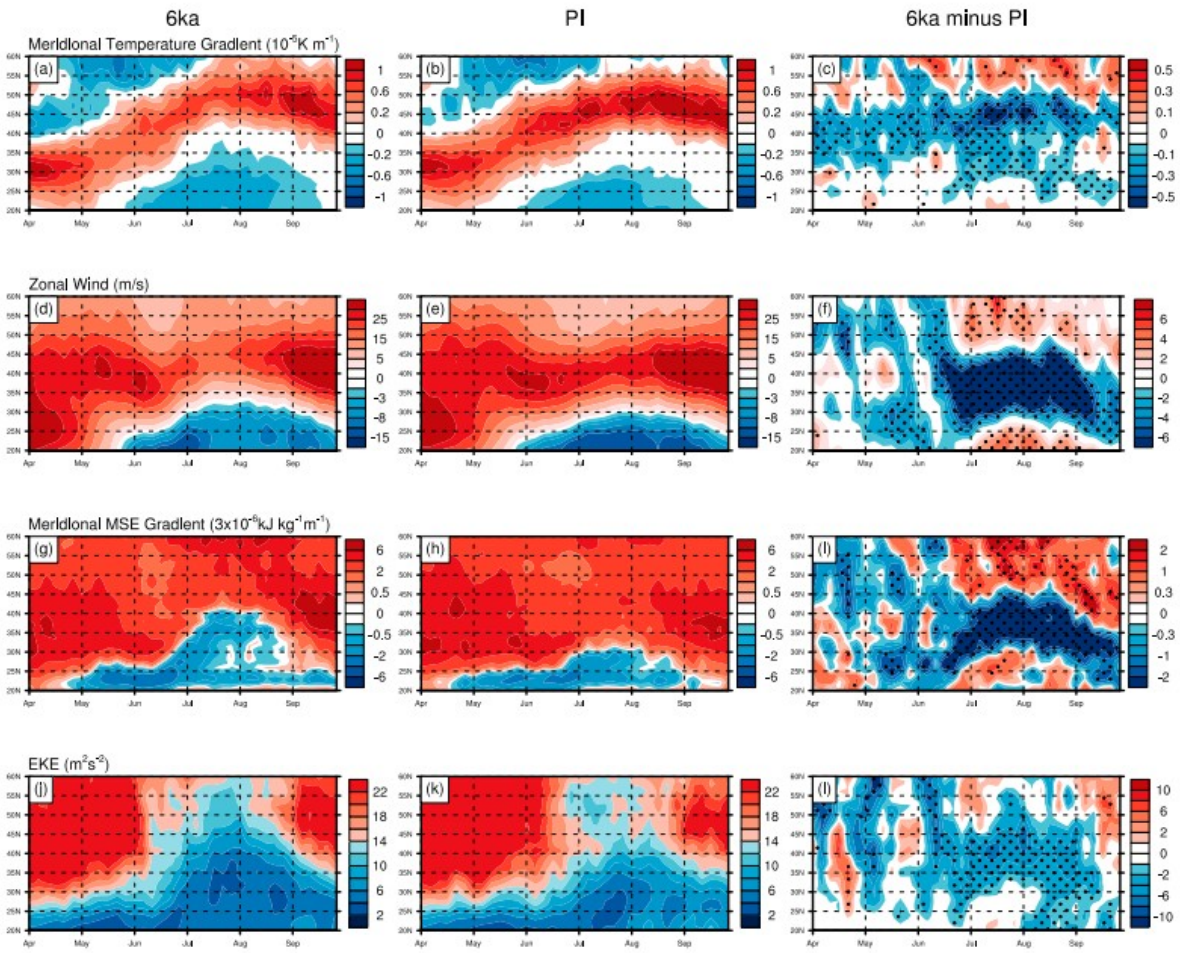

FIG. 11. Hovmöller diagrams of the (a)–(c) meridional temperature gradient (averaged over 80°–120°E) at 200 mb, (d)–(f) the zonal wind (averaged in 80°–120°E) at 200 mb, (g)–(i) the meridional gradient of MSE (averaged over 110°–120°E) between 300 and 850 mb, and (j)–(l) the eddy kinetic energy (averaged in 110°–120°E) between 300 and 850 mb, for (left) 6 ka, (middle) PI, and (right) 6 ka minus PI. The unit is 10^{-5} K^2 m^{-1} in (a)–(c), m s^{-1} in (d)–(f), 3×10^{-6} kJ^2 kg^{-1} m^{-1} in (g)–(i), and m^2 s^{-2} in (j)–(l). The stippled areas indicate that the difference is statistically significant at the confidence level of 90%.

With an earlier northward transition of the westerlies across the plateau, the frontal location will also have an earlier northward migration. We interpret the maximum meridional gradient of the MSE as the indicator of the frontal systems and Figs. 11g–i show the Hovmöller diagram of the tropospheric meridional MSE gradient $[-\partial(\mathrm{MSE})/\partial y]$ over eastern China (110°–120°E). In agreement with the changes in the transition of westerlies and rainfall band, the northward shift of the frontal systems in 6 ka is earlier and the fronts reach a more northward location.

Sampe and Xie (2010) suggest that the westerlies traps transient disturbances and these disturbances are conducive for the frontal convection. Thompson and Birner (2012), however, argue that the synoptic eddy fluxes of heat act to reduce the meridional temperature gradient. Both studies imply that the transient eddy activity is another indication of the presence of the fronts. We use the eddy kinetic energy (EKE = $u'^2 + v'^2$) to indicate transient eddy activity (Figs. 11j–l). The prime denotes 2.5–6-day

bandpass-filtered daily fields. The EKE in 6 ka (Fig. 11j) suggests an earlier northward shift of the occurrence of transient eddies, which corroborates the northward shift of the frontal systems in 6 ka.

Taken together, the weaker meridional temperature gradient and the earlier northward migration of the East Asian monsoonal fronts and associated transient eddy activity suggest that the earlier northward migration of the westerlies across the plateau, caused by the reduced meridional insolation gradient during the mid-Holocene, is responsible for the changes to the EASM seasonal transitions in the 6-ka simulation.

b. Threshold of the westerlies' position in determining the EASM seasonality

We have shown that the timing of the EASM seasonal transitions is linked to the meridional positioning of the westerlies over East Asia. We also argued (section 4c) that although the timing of the EASM seasonal stages changes across the Holocene, the dynamical configuration determining each stage remains essentially unchanged. Here we ask: Is there a physical threshold of the position of the westerlies that can exactly determine the timing of the mei-yu or midsummer onset? To answer this question, we examine the position of the westerlies across the plateau during the mei-yu onset and the midsummer onset.

Figure 12 shows the meridional position of the maximum westerlies over the Tibetan Plateau (80°–100°E) at 200 mb. Figure 12a shows that compared to the late Holocene (3 ka and PI), the northward shift of the jet axis occurs earlier in the early to mid-Holocene (9 and 6 ka), and the position of the jet axis in the early to middle Holocene is more northward displaced.

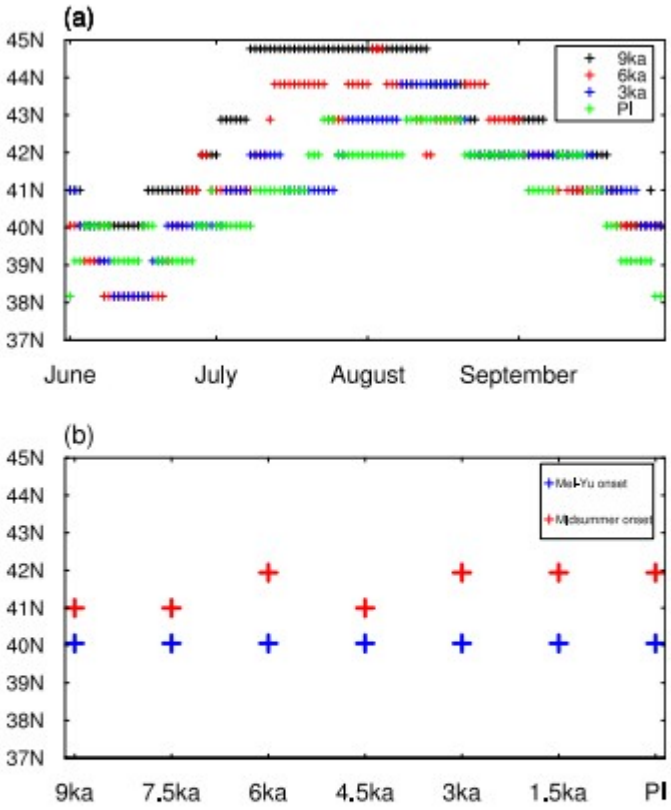

FIG. 12. (a) Meridional position of the June–September maximum zonal wind at 200 mb between 80° and 100°E in 9 ka (black crosses), 6 ka (red crosses), 3 ka (blue crosses), and PI (green crosses). (b) Meridional position of the maximum zonal wind at 200 mb between 80° and 100°E across the simulated Holocene during mei-yu onset (blue crosses) and midsummer onset (red crosses). Note that (a) is based on the daily climatology after 5-day running average, and (b) is based on the 5-day running average with the mei-yu/midsummer onset date as the center day.

Figure 12b shows that the axis of the westerlies relative to the Tibetan Plateau is located at 40°N during the mei-yu onset for all simulation cases, suggesting that this latitude acts as a threshold for triggering mei-yu onset. The left column of Fig. 13, which shows the meridional position of the maximum westerlies at mei-yu onset as a function of longitude, further confirms the consistent meridional positioning of the jet axis over the plateau longitudes at the mei-yu onset across the simulations. The position of the jet axis downstream of the plateau, though, shows some variation across the simulations. Unlike the mei-yu onset, there does not appear to be a consistent latitudinal threshold for the maximum westerlies associated with the onset of the midsummer stage. For example, Figs. 12b and 13b show that the onset of midsummer is associated with a 1° to 2° northward shift of the westerly jet axis from the mei-yu threshold position of 40°N.

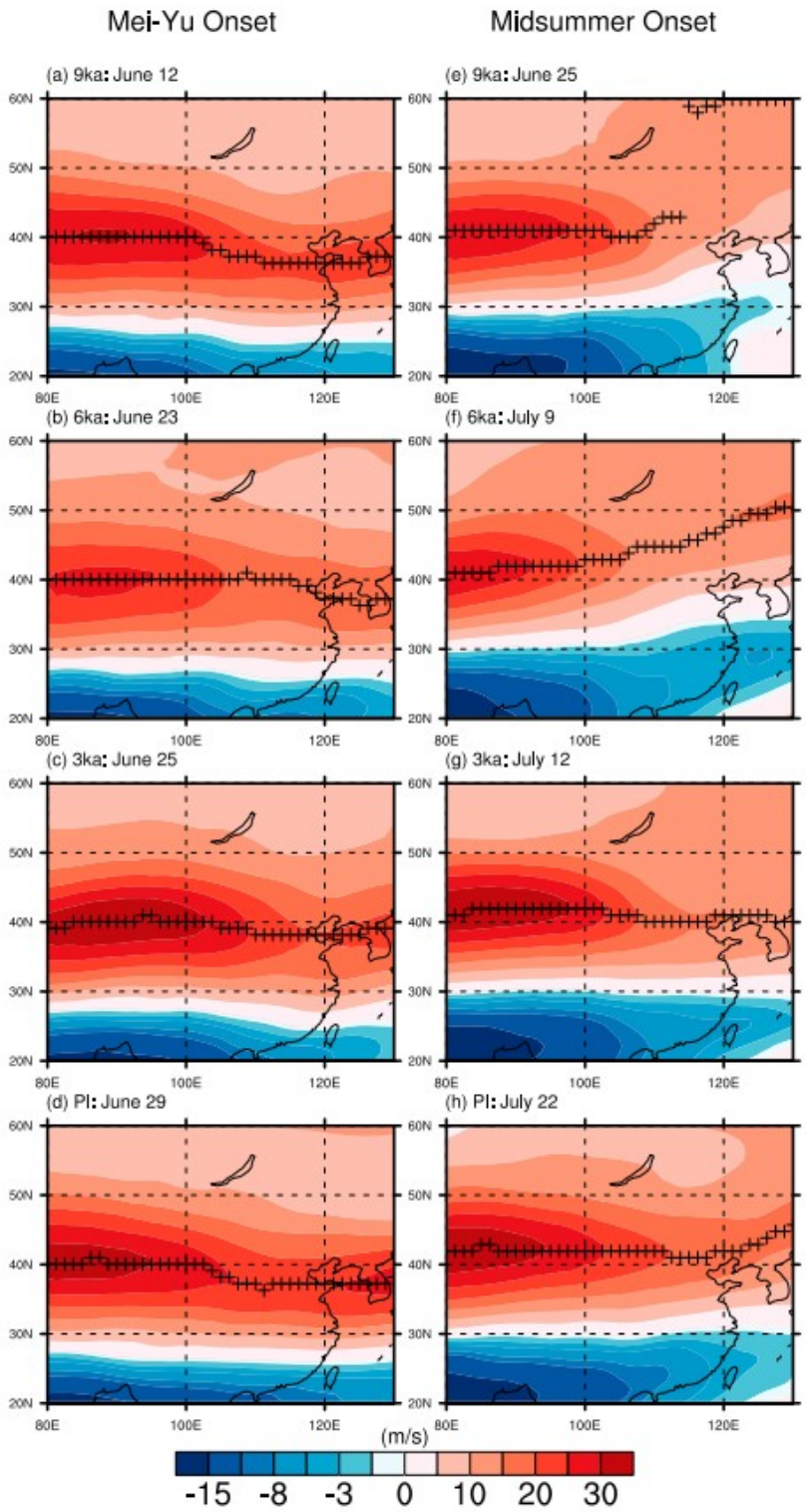

FIG. 13. (left) Zonal wind at 200 mb (warm color: westerlies; cold color: easterlies; unit: m s^{-1}) during the mei-yu onset (a) 9 ka: 12 Jun, (b) 6 ka: 23 Jun, (c) 3 ka: 25 Jun, and (d) PI: 29 Jun. (right) As at left, but for the midsummer onset (e) 9 ka: 25 Jun, (f) 6 ka: 9 Jul, (g) 3 ka: 12 Jul, and (h) PI: 22 Jul. The crosses denote the latitude position of the maximum zonal wind. For each simulation, the result is based on the 5-day average with the mei-yu/midsummer onset date as the center day.

Taken together, our simulations suggest that the mei-yu onset is linked to the maximum upper-tropospheric westerlies crossing a particular meridional position over the Tibetan region. It suggests that the position of the westerlies relative to the Tibetan Plateau provides the dynamical constraint that determines the start of mei-yu season. However, the position of the westerlies does not seem to be the deterministic factor for the midsummer onset. Therefore, we speculate that the onset process of the midsummer stage is more complex, with more than one factor playing a role. We will further explore the mechanisms associated with the onset of the mei-yu and midsummer patterns in follow-up studies.

6. Interpretation of the Holocene EASM pollen and dust records from a seasonality perspective

In this section, we further demonstrate the validity of our hypothesis by comparing our simulations with two key paleoproxy records over East Asia. We show that focusing on seasonal transitions, as opposed to the conventional focus on monsoon intensity, can provide new insights into the interpretation of these records.

a. Asynchronous Holocene optimum

Based on an interpretation of Chinese lake levels, pollen sequences, and eolian deposit records, An et al. (2000) proposed the “asynchronous Holocene optimum” hypothesis of a stepwise latitudinal shift of the maximum rainfall from northwestern China in the early Holocene (10–8 ka) to southeastern China in the late Holocene (3 ka), in response to the progressively decreased summer insolation. They argued that the weakened Northern Hemisphere insolation seasonality induces the weakening of the EASM and therefore the southward retreat of the northernmost frontal zone from the early Holocene to the late Holocene, resulting in the southward shift of the maximum rainfall belt. The view proposed by An et al. (2000) cannot be explained by the conventional interpretation of viewing paleo-EASM changes simply in terms of intensity, since it implies that the Holocene “optimum” should occur at the same time at all locations in China.

We argue that seasonal transitions provide a more satisfactory interpretation than An et al.’s (2000) result. Figure 14 presents the evolution of the EASM annual total rainfall amount (100°–120°E) (Fig. 14a) and the convective-to-total precipitation $\left(\frac{\text{convective}}{\text{total}}\right)$ ratio (Fig. 14b) from 9 ka to PI. Figure 14a shows that the simulated peak annual rainfall band shifts southward from 9 ka to PI, in agreement with the asynchronous Holocene optimum hypothesis (An et al. 2000). Moreover, Fig. 14b shows a southward shift of the peak convective-to-total precipitation ratio from 9 ka to PI, reflecting the southward displacement of the frontal systems from 9 ka to PI. Thus, we attribute the asynchronous Holocene optimum hypothesis (An et al. 2000) to the changes in both timing and duration of the EASM seasonal transition across the Holocene. In the early Holocene, the midsummer rainfall season occurs earlier and stays longer, thus the maximum annual rainfall amount

occurs over northern China (cf. Figs. 3b and 3d). In the mid-Holocene, the midsummer rainfall stage starts later and ends earlier, leading to reduced rainfall over northern China; on the other hand, the mei-yu rainfall duration is longer, leading to increased rainfall over central China, and the so-called Holocene optimal rainfall occurs there (Fig. 3c). In the late Holocene, the relatively late start of the mei-yu season determines the lengthened spring and pre-mei-yu rainfall stage, leading to more rainfall over southern China; on the other hand, the midsummer rainfall stage over northern China is further shortened, reducing the rainfall amount over northern China. The above interpretation for the asynchronous Holocene optimum hypothesis is in agreement with the schematic model summarized in Fig. 5 of Chiang et al. (2015) and is in alignment with our simulation results as well (e.g., Fig. 3).

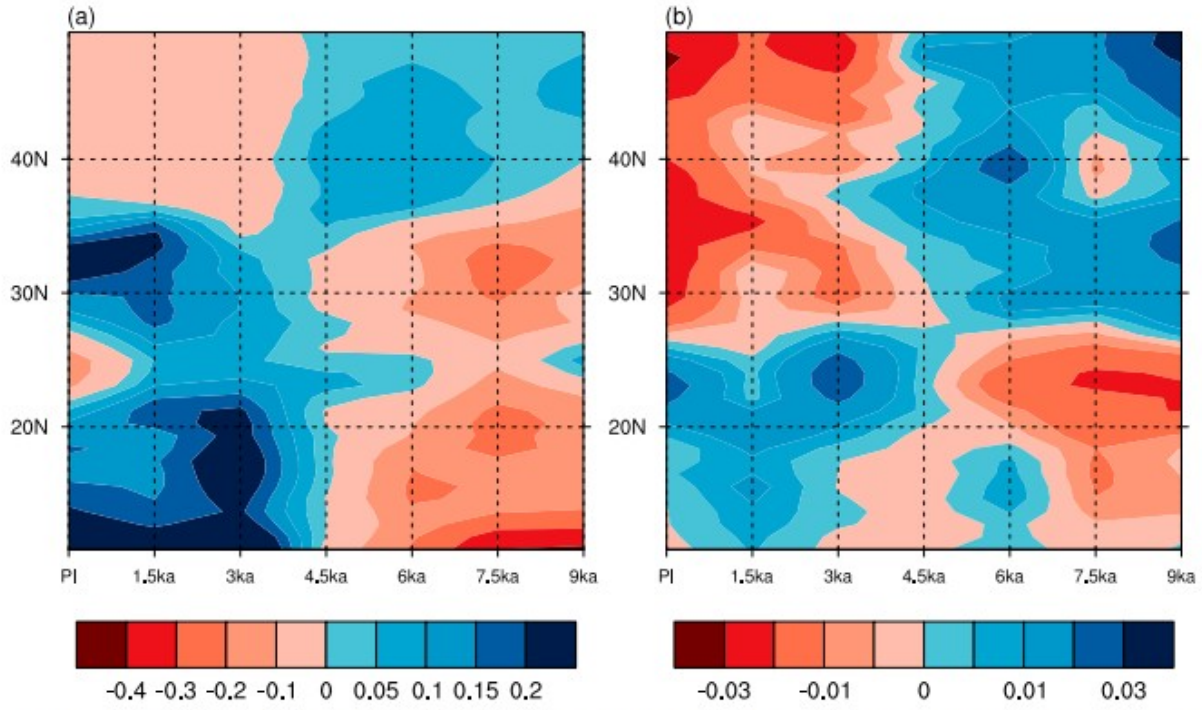

FIG. 14. (a) Annual total precipitation amount (110°–120°E) change from 9 ka to PI and (b) annual convective-to-total precipitation (convective/total) ratio change from 9 ka to PI. The convective/total ratio is calculated from proportion of convective precipitation rate to total precipitation rate between 100°and 120°E. In (a), the mean value of 9 ka to PI is removed for each simulation, cold color indicates higher annual total precipitation amount and vice versa. In (b), the mean convective/total ratio value of 9 ka to PI is removed for each simulation, cold color indicates higher convective/total ratio and vice versa.

We note that our results and interpretation differ from a recent modeling study by Jin et al. (2014). They also find regional disparity of the Holocene optimum precipitation between northeastern China and central-eastern China. However, in contrast to An et al. (2000), their modeling results suggest that the peak precipitation over central and southeastern China occurred synchronously, and earlier than that over northeastern China, leading them to conclude that “the previously-proposed time-transgressive

Holocene climate across China (e.g. An et al. 2000) is not supported by [their] study" (Jin et al. 2014, p. 58).

b. Changes to dust emissions

Dust proxies are thought to reflect changes to the westerlies in the past climate. For example, both An et al. (2012) and Nagashima et al. (2011, 2013) indicate that the enhanced dust emission over East Asia is associated with the southward-shifted westerlies during times of colder climates. Nagashima et al. (2011, 2013) hypothesized that the seasonal jet transitions from south of Tibet to the north were delayed during Dansgaard–Oeschger stadials. Given that the dust emission over East Asia mainly occurs in spring as cyclogenesis maximizes in that season (Roe 2009), the suggestion is that the dustier climate over East Asia is associated with prolonged spring rainfall season and southward-shifted westerlies.

If (as per our hypothesis) the westerlies were displaced southward and the rainfall seasonal transition was delayed in the late Holocene, we should see dustier climate during the late Holocene compared to the early to mid-Holocene; indeed, this is what our simulation shows. The monthly dust emission over the major dust outbreak region [33.5°–52°N, 88.5°–131.5°E, adapted from Kurosaki and Mikami (2003)] in PI (Fig. 15a) shows a reasonable seasonal cycle compared to observations (Kurosaki and Mikami 2003), with the exception of May when the simulated dust emission is too high. The simulated dust emission in the PI is indeed larger than that in 6 ka over East Asia (Fig. 15b). The climatological annual mean dust emission over 33.5°–52°N, 88.5°–131.5°E is 3.02 Tg m^{-2} s^{-1} in the PI and 2.78 Tg m^{-2} s^{-1} in the 6 ka, and the Student's *t* test suggests that the difference between the two is statistically significant at a confidence level of 95%.

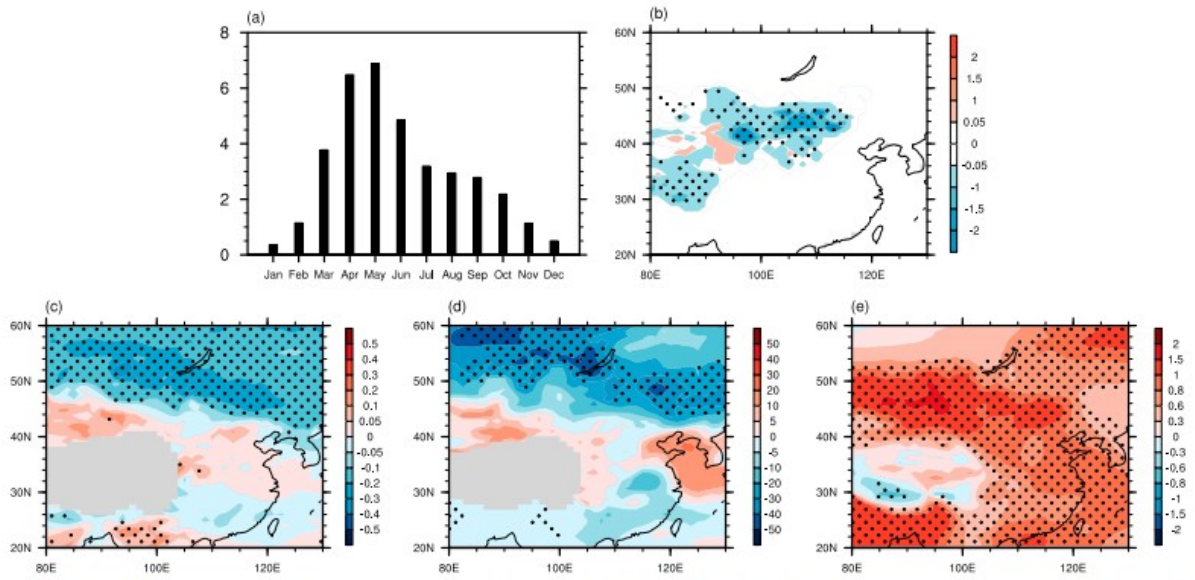

FIG. 15. (a) Monthly dust emission over high dust emission region (33.5°–52°N, 88.5°–131.5°E) from the PI simulation and (b) change of the annual mean dust emission between 6 ka and PI (6 ka minus PI). The unit is Tg m^{-2} s^{-1} in (a) and (b). Also shown is the difference between 6 ka and PI (6 ka minus PI) for MAM for (c) the meridional temperature gradient averaged over 700–1000 mb (unit: 10^{-5} K^2 m^{-1}), (d) the variance of 2.5–6 days bandpass-filtered daily geopotential height averaged over 700–1000 mb (unit: m^2), and (e) sea level pressure (unit: mb). The stippled areas indicate that the difference is statistically significant at the confidence level of 90%.

Roe (2009) suggests that the transient eddy disturbances in the atmospheric circulation and strong meridional temperature gradients are the two major prerequisites for the dust-generating windstorms. We argue that the dustier climate in the PI is due to the prolonged springtime, which is characterized by stronger meridional temperature gradient and storminess over East Asia as seen in Figs. 15c and 15d. The strength of the Siberian high in spring is thought to be negatively correlated to the dust outbreak frequency in Asia (Ding et al. 2005). Figure 15e suggests a weaker Siberian high during the PI spring, which further supports the enhanced dust emission as noted in Fig. 15b. Apart from the foregoing analyses, the delayed mei-yu onset during PI also leads to a deficit in soil moisture over the dust emission region, and thus enhances the dust lofting.

7. Conclusions and discussion

The Holocene EASM evolution, inferred from proxies such as the $\delta^{18}O_p$ records in Chinese caves (Wang et al. 2008, 2001), has been typically interpreted to be a weakening of the monsoon intensity from the early Holocene to the present day. Given that today's EASM is characterized by three distinct seasonal regimes and abrupt transitions in between, this interpretation is incomplete and a fuller account of the Holocene EASM changes must include the changes to these seasonal transitions. In this study, we investigate the changes in the seasonal transitions of the EASM during the Holocene based on the simulation from CAM5 that is capable of simulating today's seasonal transitions with fidelity. Following a previous lead (Chiang et al. 2015), we test the hypothesis that the changes in the

seasonal transition of the Holocene EASM are determined by the altered position of the westerly jet relative to the Tibetan Plateau.

We explored the Holocene EASM in a set of CAM5 simulations spanning various time periods in the Holocene (9, 7.5, 6, 4.5, 3, 1.5 ka, and PI). We showed that compared to the late Holocene, the early to mid-Holocene is characterized by an earlier onset of the mei-yu and midsummer rainfall seasons, with a shorter duration of mei-yu and longer duration of midsummer. In particular, the simulations suggest that the midsummer stage was twice the duration and the mei-yu half the duration during the early Holocene as in the present. In confirmation of the altered seasonality of the EASM, the early to mid-Holocene also featured northward-shifted mei-yu and midsummer rainfall fronts as well as more northward penetration of the moisture flux. The meridional position of the high cyclonic vorticity and the moisture convergence further corroborates the above interpretation. It should be mentioned that we obtained similar results—namely, that the mid-Holocene featured earlier EASM seasonal transition than the preindustrial—from four PMIP3 models (CCSM4, BCC-CSM1.1, FGOALS-g2, FGOALS-s2) that are able to simulate the EASM with fidelity (see the appendix).

In terms of the role of the westerlies, the northward positioning of the westerlies relative to the Tibetan Plateau in the early Holocene appears linked to the earlier timing of the seasonal transitions. The insolation over the Northern Hemisphere summer was increased in the early Holocene, leading to a northward shift in the maximum meridional temperature gradient and hence the westerlies. Transient eddies over East Asia are also northward shifted in the early to mid-Holocene, further indicating the northward displacement of the frontal systems during that time. Our analysis suggests the existence of specific thresholds (40°N) in the meridional position of the westerlies over the Tibetan region (80°–100°E) that controls the mei-yu onset across the Holocene. This is not true, however, for the midsummer stage onset.

The mei-yu and midsummer rainfall stages in the early to mid-Holocene appear more intense than their counterparts in the late Holocene. This is also associated with the more northward positioned westerlies in the early to mid-Holocene. However, the underlying dynamics of the EASM in the early to mid-Holocene and the late Holocene resemble each other qualitatively.

We also compare our simulations against two well-known paleoproxy studies of the East Asian paleoclimate and offer an interpretation based on the seasonal transition perspective. In agreement with the “asynchronous Holocene optimum” hypothesis (An et al. 2000), the simulated changes in the annual rainfall amount and the $(\text{convective/total})$ ratio over East Asia suggest that the latitudinal position of the maximum rainfall band moves southward from the early Holocene to the late Holocene. We argue that this phenomenon is readily interpretable if we consider that the seasonal transitions from spring/pre-mei-yu to mei-yu and from mei-yu to midsummer

occurred later as the Holocene progressed. We also find that the simulated late Holocene is dustier than the mid-Holocene over East Asia, which is consistent with the argument that the enhanced dust emission over East Asia is associated with the southward-shifted westerlies during colder climate (An et al. 2012; Nagashima et al. 2011, 2013). Given that the dust emission over East Asia is mainly a springtime phenomenon (Roe 2009), the dustier late Holocene is a further confirmation of the delayed onset of the mei-yu (i.e., the prolonged spring/pre-mei-yu rainfall season).

It is not the purpose of this paper to fully elucidate the mechanistic links between the westerlies and the EASM seasonality. The overarching question that we will explore in future studies is this: what characteristics of the westerlies are most relevant to each seasonal stage of EASM? Besides the meridional positioning of the westerlies, the potential candidates include the width, the vertical structure, and the strength of the westerlies. During the transition from spring to pre-mei-yu, the westerlies shift poleward from southern China to the south edge of the Tibetan Plateau (Schiemann et al. 2009); however, the meridional positioning of the rainfall over southern China between spring and pre-mei-yu is similar (Fig. 1). The strength as well as the westward extension of the pre-mei-yu rain belt, however, is intensified. Unlike the difference between mei-yu and midsummer rainfall, the northward shift of the westerlies does not affect the meridional position of the rain belt during the transition from spring to pre-mei-yu. For the mei-yu onset, our analysis suggests that the meridional positioning (40°N) of the westerlies axis at 200 mb relative to the Tibetan Plateau is a strong determinant thereof, but this needs further examination. Specifically, what are the specific dynamics that determine why the mei-yu onset occurs at this latitude? A latitudinal threshold does not appear to hold for the midsummer onset, and this begs the question of whether there are other factors that affect the onset of the midsummer stage.

There are still fundamental questions to be answered regarding the role of stationary eddies and transient eddies associated with westerly atmospheric circulation across East Asia. Stationary eddies downstream of the Tibetan Plateau are thought to be the main factor for the formation and maintenance of the East Asian monsoon front by converging warm, moist air from the south with the cold, dry air from the north (Staff 1957). Therefore, we postulate that the westerlies exert a modulation of the seasonality of the EASM via controlling the behavior of the stationary eddies downstream of the plateau. The role of the transient eddies in the EASM seasonality is not yet fully understood. On one hand, the transient eddies are argued to smooth out the meridional temperature gradient (Thompson and Birner 2012); on the other hand, Sampe and Xie (2010) suggest that the transient disturbances trapped along the westerlies facilitate the mei-yu frontal convection.

Acknowledgments

We thank Nathaniel Johnson for sharing his SOMs analysis code, and Shing Chang for her assistance in implementation. Mike Wallace suggested the use of SOMs to analyze East Asian rainfall seasonality. We thank Chi-Hua Wu, Inez Y. Fung, and Yanjun Cai for valuable discussions. We thank Dr. Mathew Barlow and the three anonymous reviewers for their constructive comments. WK thanks Jun Yang for helpful conversations on the use of the Community Earth System Model. APHRODITE precipitation data were obtained from http://www.chikyu.ac.jp/precip/index.html. We thank the Paleoclimate Modelling Intercomparison Project Phase III (PMIP3) for producing and making available their model output. We acknowledge high-performance computing support for the CAM5 from the Yellowstone cluster (ark:/85065/d7wd3xhc) provided by NCAR's Computational and Information Systems Laboratory, sponsored by the National Science Foundation. We use the NCAR Command Language (http://www.ncl.ucar.edu) to perform the calculation and visualization, and MATLAB (http://www.mathworks.com/products/matlab/) to perform the self-organizing maps (SOMs) analysis. This work was funded by National Science Foundation Grant AGS-1405479.

REFERENCES

An, Z., S. C. Porter, J. E. Kutzbach, X. Wu, S. Wang, X. Liu, X. Li, and W. Zhou, 2000: Asynchronous Holocene optimum of the East Asian monsoon. *Quat. Sci. Rev.*, 19, 743–762, doi:https://doi.org/10.1016/S0277-3791(99)00031-1.

An, Z., and Coauthors, 2012: Interplay between the westerlies and Asian monsoon recorded in Lake Qinghai sediments since 32 ka. *Sci. Rep.*, 2, 619, doi:https://doi.org/10.1038/srep00619.

Bao, M., and J. M. Wallace, 2015: Cluster analysis of Northern Hemisphere wintertime 500-hPa flow regimes during 1920–2014. *J. Atmos. Sci.*, 72, 3597–3608, doi:https://doi.org/10.1175/JAS-D-15-0001.1.

Bao, Q., and Coauthors, 2013: The Flexible Global Ocean–Atmosphere–Land System Model, spectral version 2: FGOALS-s2. *Adv. Atmos. Sci.*, 30, 561–576, doi:https://doi.org/10.1007/s00376-012-2113-9.

Berger, A., M.-F. Loutre, and C. Tricot, 1993: Insolation and Earth's orbital periods. *J. Geophys. Res.*, 98, 10 341–10 362, doi:https://doi.org/10.1029/93JD00222.

Braconnot, P., S. P. Harrison, M. Kageyama, P. J. Bartlein, V. Masson-Delmotte, A. Abe-Ouchi, B. Otto-Bliesner, and Y. Zhao, 2012: Evaluation of climate models using palaeoclimatic data. *Nat. Climate Change*, 2, 417–424, doi:https://doi.org/10.1038/nclimate1456.

Chang, C.-H., and N. C. Johnson, 2015: The continuum of wintertime Southern Hemisphere atmospheric teleconnection patterns. *J. Climate*, 28, 9507–9529, doi:https://doi.org/10.1175/JCLI-D-14-00739.1.

Chattopadhyay, R., A. K. Sahai, and B. N. Goswami, 2008: Objective identification of nonlinear convectively coupled phases of monsoon intraseasonal oscillation: Implications for prediction. *J. Atmos. Sci.*, 65, 1549–1569, doi:https://doi.org/10.1175/2007JAS2474.1.

Chen, J., and S. Bordoni, 2014: Orographic effects of the Tibetan Plateau on the East Asian summer monsoon: An energetic perspective. *J. Climate*, 27, 3052–3072, doi:https://doi.org/10.1175/JCLI-D-13-00479.1.

Chen, S.-J., Y.-H. Kuo, W. Wang, Z.-Y. Tao, and B. Cui, 1998: A modeling case study of heavy rainstorms along the mei-yu front. *Mon. Wea. Rev.*, 126, 2330–2351, doi:https://doi.org/10.1175/1520-0493(1998)126<2330:AMCSOH>2.0.CO;2.

Chiang, J. C. H., and Coauthors, 2015: Role of seasonal transitions and westerly jets in East Asian paleoclimate. *Quat. Sci. Rev.*, 108, 111–129, doi:https://doi.org/10.1016/j.quascirev.2014.11.009.

Chu, J.-E., S. N. Hameed, and K.-J. Ha, 2012: Nonlinear, intraseasonal phases of the East Asian summer monsoon: Extraction and analysis using self-organizing maps. *J. Climate*, 25, 6975–6988, doi:https://doi.org/10.1175/JCLI-D-11-00512.1.

Dansgaard, W., 1964: Stable isotopes in precipitation. *Tellus*, 16, 436–468, doi:https://doi.org/10.3402/tellusa.v16i4.8993.

Ding, R., J. Li, S. Wang, and F. Ren, 2005: Decadal change of the spring dust storm in northwest China and the associated atmospheric circulation. *Geophys. Res. Lett.*, 32, L02808, doi:https://doi.org/10.1029/2004GL021561.

Ding, Y., and J. C. L. Chan, 2005: The East Asian summer monsoon: An overview. *Meteor. Atmos. Phys.*, 89, 117–142, doi:https://doi.org/10.1007/s00703-005-0125-z.

Gent, P. R., and Coauthors, 2011: The Community Climate System Model version 4. *J. Climate*, 24, 4973–4991, doi:https://doi.org/10.1175/2011JCLI4083.1.

Han, Z., and T. Zhou, 2012: Assessing the quality of APHRODITE high-resolution daily precipitation dataset over contiguous China. *Chin. J. Atmos. Sci.*, 36, 361–373.

Hurrell, J. W., and Coauthors, 2013: The Community Earth System Model: A framework for collaborative research. *Bull. Amer. Meteor. Soc.*, 94, 1339–1360, doi:https://doi.org/10.1175/BAMS-D-12-00121.1.

Iskandar, I., 2009: Variability of satellite-observed sea surface height in the tropical Indian Ocean: Comparison of EOF and SOM analysis. *Makara J. Sci.*, 13, 173–179, doi:https://doi.org/10.7454/mss.v13i2.421.

Jin, L., B. Schneider, W. Park, M. Latif, V. Khon, and X. Zhang, 2014: The spatial–temporal patterns of Asian summer monsoon precipitation in

response to Holocene insolation change: A model-data synthesis. *Quat. Sci. Rev.*, 85, 47–62, doi:https://doi.org/10.1016/j.quascirev.2013.11.004.

Johnson, N. C., 2013: How many ENSO flavors can we distinguish? *J. Climate*, 26, 4816–4827, doi:https://doi.org/10.1175/JCLI-D-12-00649.1.

Johnson, N. C., S. B. Feldstein, and B. Tremblay, 2008: The continuum of Northern Hemisphere teleconnection patterns and a description of the NAO shift with the use of self-organizing maps. *J. Climate*, 21, 6354–6371, doi:https://doi.org/10.1175/2008JCLI2380.1.

Kohonen, T., 2001: *Self-Organizing Maps*. Springer, 502 pp.

Kohonen, T., J. Hynninen, J. Kangas, and J. Laaksonen, 1996: SOM_PAK: The self-organizing maps program package. Tech. Rep. A31, Helsinki University of Technology, Laboratory of Computer and Information Science, 25 pp.

Kurosaki, Y., and M. Mikami, 2003: Recent frequent dust events and their relation to surface wind in East Asia. *Geophys. Res. Lett.*, 30, 1736, doi:https://doi.org/10.1029/2003GL017261.

Lau, K.-M., G. J. Yang, and S. H. Shen, 1988: Seasonal and intraseasonal climatology of summer monsoon rainfall over East Asia. *Mon. Wea. Rev.*, 116, 18–37, doi:https://doi.org/10.1175/1520-0493(1988)116<0018:SAICOS>2.0.CO;2.

Li, C., and M. Yanai, 1996: The onset and interannual variability of the Asian summer monsoon in relation to land–sea thermal contrast. *J. Climate*, 9, 358–375, doi:https://doi.org/10.1175/1520-0442(1996)009<0358:TOAIVO>2.0.CO;2.

Li, L., and Coauthors, 2013: The Flexible Global Ocean–Atmosphere–Land System Model, grid-point version 2: FGOALS-g2. *Adv. Atmos. Sci.*, 30, 543–560, doi:https://doi.org/10.1007/s00376-012-2140-6.

Liang, X.-Z., and W.-C. Wang, 1998: Associations between China monsoon rainfall and tropospheric jets. *Quart. J. Roy. Meteor. Soc.*, 124, 2597–2623, doi:https://doi.org/10.1002/qj.49712455204.

Lin, G.-F., and L.-H. Chen, 2006: Identification of homogeneous regions for regional frequency analysis using the self-organizing map. *J. Hydrol.*, 324, 1–9, doi:https://doi.org/10.1016/j.jhydrol.2005.09.009.

Liu, Y., R. H. Weisberg, and C. N. K. Mooers, 2006: Performance evaluation of the self-organizing map for feature extraction. *J. Geophys. Res.*, 111, C05018, doi:https://doi.org/10.1029/2005JC003117 .

Molnar, P., W. R. Boos, and D. S. Battisti, 2010: Orographic controls on climate and paleoclimate of Asia: Thermal and mechanical roles for the Tibetan Plateau. *Annu. Rev. Earth Planet. Sci.*, 38, 77–102, doi:https://doi.org/10.1146/annurev-earth-040809-152456.

Nagashima, K., R. Tada, A. Tani, Y. Sun, Y. Isozaki, S. Toyoda, and H. Hasegawa, 2011: Millennial-scale oscillations of the westerly jet path during the last glacial period. *J. Asian Earth Sci.*, 40, 1214–1220, doi:https://doi.org/10.1016/j.jseaes.2010.08.010.

Nagashima, K., R. Tada, and S. Toyoda, 2013: Westerly jet–East Asian summer monsoon connection during the Holocene. *Geochem. Geophys. Geosyst.*, 14, 5041–5053, doi:https://doi.org/10.1002/2013GC004931.

Ninomiya, K., 1984: Characteristics of Baiu front as a predominant subtropical front in the summer northern hemisphere. *J. Meteor. Soc. Japan*, 62, 880–894.

Roe, G., 2009: On the interpretation of Chinese loess as a paleoclimate indicator. *Quat. Res.*, 71, 150–161, doi:https://doi.org/10.1016/j.yqres.2008.09.004.

Sampe, T., and S.-P. Xie, 2010: Large-scale dynamics of the meiyu–baiu rainband: Environmental forcing by the westerly jet. *J. Climate*, 23, 113–134, doi:https://doi.org/10.1175/2009JCLI3128.1.

Schiemann, R., D. Lüthi, and C. Schär, 2009: Seasonality and interannual variability of the westerly jet in the Tibetan Plateau region. *J. Climate*, 22, 2940–2957, doi:https://doi.org/10.1175/2008JCLI2625.1.

Shi, Z., 2016: Response of Asian summer monsoon duration to orbital forcing under glacial and interglacial conditions: Implication for precipitation variability in geological records. *Quat. Sci. Rev.*, 139, 30–42, doi:https://doi.org/10.1016/j.quascirev.2016.03.008.

Solidoro, C., V. Bandelj, P. Barbieri, G. Cossarini, and S. Fonda Umani, 2007: Understanding dynamic of biogeochemical properties in the northern Adriatic Sea by using self-organizing maps and k-means clustering. *J. Geophys. Res.*, 112, C07S90, doi:https://doi.org/10.1029/2006JC003553.

Staff, 1957: On the general circulation over eastern Asia (I). *Tellus*, 9, 432–446. [The complete “author” as given in print for Staff (1957) and Staff (1958a,b) is “Staff Members of the Section of Synoptic and Dynamic Meteorology, Institute of Geophysics and Meteorology, Academia Sinica, Peking”; no individual authors were listed.]

Staff, 1958a: On the general circulation over eastern Asia (II). *Tellus*, 10, 58–75.

Staff, 1958b: On the general circulation over eastern Asia (III). *Tellus*, 10, 299–312.

Tao, S., and L. Chen, 1987: A review of recent research on the East Asian summer monsoon in China. *Monsoon Meteorology*, C.-P. Chang and T. N. Krishnamurti, Eds., Oxford University Press, 60–92.

Thompson, D. W. J., and T. Birner, 2012: On the linkages between the tropospheric isentropic slope and eddy fluxes of heat during Northern Hemisphere winter. *J. Atmos. Sci.*, 69, 1811–1823, doi:https://doi.org/10.1175/JAS-D-11-0187.1.

Tomita, T., T. Yamaura, and T. Hashimoto, 2011: Interannual variability of the baiu season near Japan evaluated from the equivalent potential temperature. *J. Meteor. Soc. Japan*, 89, 517–537, doi:https://doi.org/10.2151/jmsj.2011-507.

Wang, B., and LinHo, 2002: Rainy season of the Asian–Pacific summer monsoon. *J. Climate*, 15, 386–398, doi:https://doi.org/10.1175/1520-0442(2002)015<0386:RSOTAP>2.0.CO;2.

Wang, Y., H. Cheng, R. L. Edwards, Z. An, J. Wu, C.-C. Shen, and J. Dorale, 2001: A high-resolution absolute-dated late Pleistocene monsoon record from Hulu Cave, China. *Science*, 294, 2345–2348, doi:https://doi.org/10.1126/science.1064618.

Wang, Y., and Coauthors, 2005: The Holocene Asian monsoon: Links to solar changes and North Atlantic climate. *Science*, 308, 854–857, doi:https://doi.org/10.1126/science.1106296.

Wang, Y., and Coauthors, 2008: Millennial- and orbital-scale changes in the East Asian monsoon over the past 224,000 years. *Nature*, 451, 1090–1093, doi:https://doi.org/10.1038/nature06692.

Wu, G., and Coauthors, 2007: The influence of mechanical and thermal forcing by the Tibetan Plateau on Asian climate. *J. Hydrometeor.*, 8, 770–789, doi:https://doi.org/10.1175/JHM609.1.

Wu, T., and Coauthors, 2013: Global carbon budgets simulated by the Beijing Climate Center Climate System Model for the last century. *J. Geophys. Res. Atmos.*, 118, 4326–4347, doi:https://doi.org/10.1002/jgrd.50320.

Xu, W., and E. J. Zipser, 2011: Diurnal variations of precipitation, deep convection, and lightning over and east of the eastern Tibetan Plateau. *J. Climate*, 24, 448–465, doi:https://doi.org/10.1175/2010JCLI3719.1.

Yanai, M., and G.-X. Wu, 2006: Effects of the Tibetan Plateau. *The Asian Monsoon*, B. Wang, Ed., Springer, 513–549.

Yatagai, A., O. Arakawa, K. Kamiguchi, H. Kawamoto, M. I. Nodzu, and A. Hamada, 2009: A 44-year daily gridded precipitation dataset for Asia based on a dense network of rain gauges. *SOLA*, 5, 137–140, doi:https://doi.org/10.2151/sola.2009-035.

Yatagai, A., K. Kamiguchi, O. Arakawa, A. Hamada, N. Yasutomi, and A. Kitoh, 2012: APHRODITE: Constructing a long-term daily gridded precipitation dataset for Asia based on a dense network of rain gauges. *Bull. Amer. Meteor. Soc.*, 93, 1401–1415, doi:https://doi.org/10.1175/BAMS-D-11-00122.1.

Yeh, T.-C., S.-Y. Dao, and M.-T. Li, 1959: The abrupt change of circulation over the Northern Hemisphere during June and October. *The Atmosphere and the Sea in Motion*, B. Bolin, Ed., Rockefeller Institute Press, 249–267. Google Scholar

Zheng, W., B. Wu, J. He, and Y. Yu, 2013: The East Asian summer monsoon at mid-Holocene: Results from PMIP3 simulations. *Climate Past*, 9, 453–466, doi:https://doi.org/10.5194/cp-9-453-2013.

APPENDIX

The Seasonal Transition of EASM in the 6-ka and PI Simulations from PMIP3

The results of our analysis were derived solely from simulations of one atmospheric general circulation model (CAM5). To test our hypothesis using more realistic coupled model simulations, we analyze the standard preindustrial (PI) and mid-Holocene (6 ka) simulations from the PMIP3 models (Braconnot et al. 2012). Although the ensemble mean of the PI reproduces the spatial pattern of summer monsoonal rainfall (Zheng et al. 2013) at a gross level, GCMs generally fail to simulate the fine structure of the EASM seasonal evolution. Our own analysis reveals that only four models—CCSM4 (Gent et al. 2011), BCC-CSM1.1 (Wu et al. 2013), FGOALS-g2 (Li et al. 2013), and FGOALS-s2 (Bao et al. 2013)—out of the 13 that we analyze are able to simulate the seasonal transition of EASM in the PI simulation with fidelity (Figs. A1e–h). Note that the timing of the mei-yu onset in these models is delayed compared with the present day (Fig. 1), and a disparity in the intensity and timing of the EASM is evident among the four models (Figs. A1e–h). Basic information on the four models is listed in Table A1.

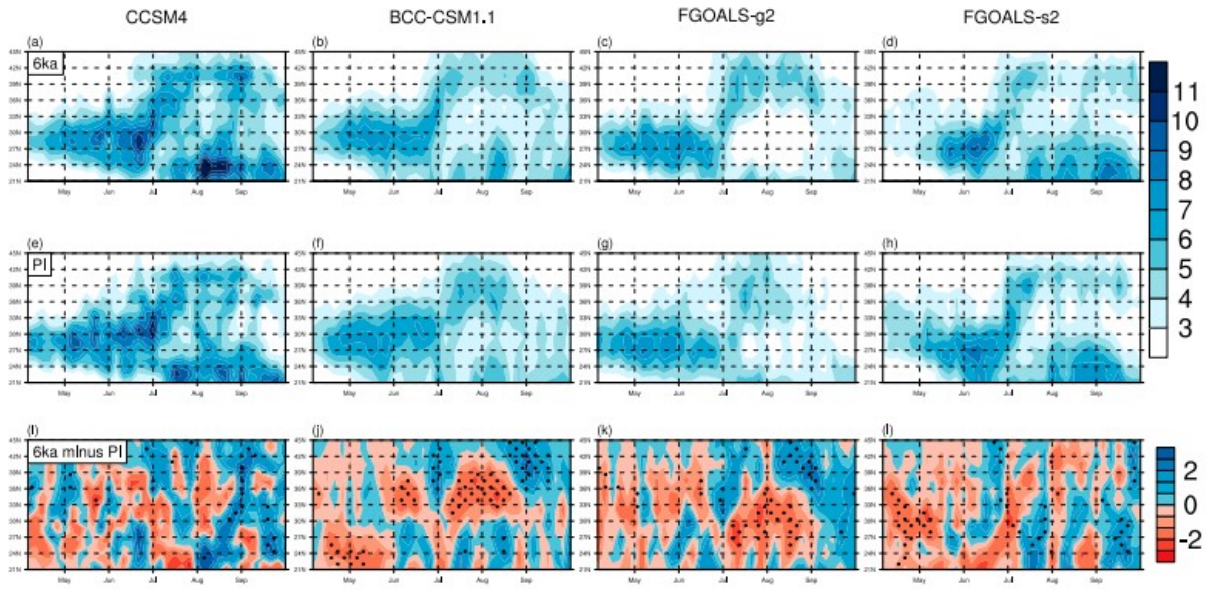

FIG. A1. Hovmöller diagram of precipitation (110°–120°E) from CCSM4, BCC-CSM1.1, FGOALS-g2, and FGOALS-s2, for (top) the 6-ka simulations and (middle) the PI simulations, and (bottom) 6 ka minus PI. Unit is mm day^{-1}. The stippled areas indicate that the difference is statistically significant at the confidence level of 90%.

TABLE A1. Basic information for the four PMIP3 models. (Expansions of acronyms are available online at http://www.ametsoc.org/PubsAcronymList.)

Model	Atmospheric resolution (lat × lon)	Length of analyzed outputs (yr) 6 ka	PI	References
BCC-CSM1.1	64 × 128	100	100	Wu et al. (2013)
CCSM4	192 × 288	32	20	Gent et al. (2011)
FGOALS-g2	60 × 128	30	40	Li et al. (2013)
FGOALS-s2	108 × 128	50	50	Bao et al. (2013)

Compared with PI, it is visually apparent in the precipitation field that the 6-ka simulations in each of these four models possess an earlier onset of mei-yu and midsummer, and longer duration of midsummer stage (Figs. A1a–d). The difference (6 ka minus PI) (Figs. A1i–l) suggests a “wet north and dry south” pattern around late June and early July, indicating an earlier onset of mei-yu in 6 ka. The overall wet north and dry south pattern persists from late June to mid-September in CCSM4, BCC-CSM1.1, and FGOALS-g2 (Figs. A1i–k), suggesting that the midsummer pattern starts earlier and persists longer over northern China in the 6-ka simulations. Note that for FGOALS-s2 the deficit in the July–August rainfall over northern China (Fig. A1l) is mainly due to the reduced intensity of midsummer rainfall in 6 ka (Fig. A1d). Figure A2 shows the zonal wind over East Asia in summer (JJA), based on the multimodel ensemble mean from the four models. All the model outputs are interpolated onto the same grid as CCSM4 using bilinear interpolation. The 6-ka minus PI difference (color shading in Fig. A2) features strengthened westerlies on the northern flank of the PI jet core (contour in Fig. A2) and weakened westerlies on the southern flank of the PI jet core, suggesting an earlier northward shift of westerlies in the simulated mid-Holocene. These results further support our argument that a northward shift of the westerlies in the early to mid-Holocene led to an earlier seasonal transition of EASM during that time.

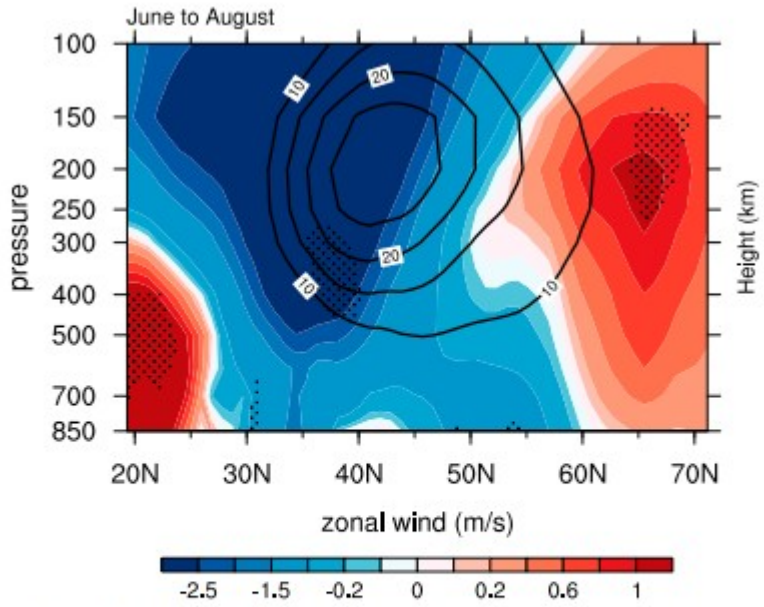

FIG. A2. JJA zonal wind (80°–120°E) from the multimodel ensemble mean of CCSM4, BCC-CSM1.1, FGOALS-g2, and FGOALS-s2 (contour: PI; shading: 6 ka minus PI; unit: m s^{-1}). The stippled areas indicate that the difference is statistically significant at the confidence level of 90%.